

Doctoral Thesis Reviewed
by Ritsumeikan University

Hall-Effect-Based Soft Tactile Fingertips for
Assembly Tasks

(ホール効果に基づいた組立作業のための
柔軟触覚センサ)

March 2020
2020年3月

Doctoral Program in Advanced Mechanical Engineering
and Robotics

Graduate School of Science and Engineering
Ritsumeikan University

立命館大学大学院理工学研究科

機械システム専攻博士課程後期課程

MUHAMMAD Hisyam Bin Rosle

ムハンマド ヒシャム ビン ロスレ

Supervisor: Professor HIRAI Shinichi

研究指導教員：平井 慎一教授

Abstract

A soft fingertip with tactile sensation was proposed to provide tactile information in manipulating assembly parts. The grasping information such as object orientation and grasping force are essential before assembly tasks to assist the manipulators. Moreover, the contact states between the handled objects and the environment vary as the assembling operation proceeds. Thus, an estimation contact state method is required to reconstruct robotic motion for successful assembly. However, designing a tactile fingertip with a simple structure that can generate such tactile information is a challenging task.

In this study, a simple structured of Hall effect-based soft tactile fingertip applied to robotic gripper for assembly tasks is proposed. The fingertip is sensitive to external forces and able to estimate object orientation, gripping force, and contact states between the grasped objects and the environment. Four cylindrical neodymium magnets were embedded in the soft body, and two 3-axis Hall sensors were fixed at the fingertip base. A machine learning approach, i.e. feedforward neural network, was applied to clarify the relationship between the changes of magnetic flux density (MFD) measured by Hall sensors and the target outputs.

Then, the finite element of simulations was performed to investigate the sensor performance to discriminate different contact states. The fingertip model with the proposed arrangement of magnets and Hall element was constructed in

a simulator. Simulation results present that the simulated MFD changes were distributed in different separated regions for three different predefined contact states. The simulation result shows that the fingertip design was able to generate enough features to classify the contact states.

The fingertip was fabricated with the same parameters in simulation, and it was tested to estimate object orientation and gripping force of thin circuit boards. The board was set to different orientations with various contact positions through fingertip surface. We found that, even the grasping task were conducted with untrained contact position, the fingertip was able to estimate object orientation within the range $\pm 5^\circ$, and the grasping force within the threshold of ± 1.5 N. We also found that the estimation error was slightly increased with the increase in board thickness. Then, the classification test of the contact state was performed with a thin circuit board and an electrical inverter. The classification result shows that the classification probabilities were over 90% accuracy. It validated that the neural network can successfully classify the contact states, even with the untrained contact direction, grasping position, and flange orientation.

Acknowledgments

I would like to thank everyone who contributed to this dissertation. With deep gratitude, I would like to thank my supervisor, Professor Shinichi Hirai for supervising me during doctoral degree program. He has contributed a great deal of ideas, guidance, support, *etc.* in Soft Robotics Laboratory.

In addition, I would like to thank Professor Sadao Kawamura for giving opinion regarding the tactile system for parts assembly. It is a good experience to work in collaboration with his laboratory members. I also much appreciate Professor Shimonomura, who always give supportive advice during a joint seminar presentation at Ritsumeikan University.

I also would like to thank Associate Professor Zhongkui Wang, who has given me a lot of help and advice about finite element simulation and experiments. I also am grateful to have Dr. Keung Or, who has advised and supported me in my research. Special thanks to Mr. Okino who has given me valuable advice and guidance during the discussion to construct a ROS environment using Denso Robot. Many thanks to my research team, Tactile Sensor Group of Hirai Lab, for their support and friendship. A very special gratitude to all Hirai Lab members who have supported me along the way. It was a great sharing laboratory with all of you during the last 3 years.

I am deeply grateful to my family, who have extended their love, positive support, encouragement during my study. Without their understanding, it is difficult to achieve my dream.

Lastly, I would like to thank the Malaysia Japan Higher Education Program (MJHEP) of the government of Malaysia for providing the scholarship.

Table of Contents

Abstract	i
Acknowledgments	iii
Table of Contents	v
List of figures	viii
List of Tables	xiii
CHAPTER 1. Introduction	1
1.1 Soft tactile sensors in robotic systems.....	3
1.2 Modeling of soft tactile fingertip.....	6
1.3 Contact state estimation in assembly tasks.....	7
1.4 Research objectives	7
1.5 Dissertation organizations	8
CHAPTER 2. Design and Modeling of Soft Fingertip	10
2.1 Design principle	10
2.2 Finite element simulation	12
2.2.1 Simulating deformation.....	13
2.2.2 Magnetic field simulation	15

2.2.3	Simulation results.....	17
2.3	Fabrication of soft fingertip.....	17
2.4	Hysteresis test.....	20
CHAPTER 3. System Configuration and Equipment.....		23
3.1	Introduction	23
3.2	Tactile system.....	23
3.3	Feedback control system	25
CHAPTER 4. Experimental Test of Object Orientation and		
Gripping Force Estimation		27
4.1	Calibration procedure	27
4.2	Validation tests	31
4.3	Results and discussion.....	32
CHAPTER 5. Classification of Contact State		36
5.1	Thin rectangular object.....	36
5.1.1	Calibration procedure.....	36
5.1.2	Assessment tests.....	39
5.2	Electrical inverter	42
5.2.1	Calibration setup	42
5.2.2	Assessment tests.....	47

5.3 Experimental test of part assembly condition classification and
feedback control60

5.3.1 Feedback of false insertion detection60

5.3.2 Application with a visual feedback system.....63

5.4 Discussion67

CHAPTER 6. Conclusion and Future Works.....69

6.1 Conclusions69

6.2 Future works.....72

References73

List of Figures

Figure 1. Arrangement of magnets and Hall sensors in the exploded view. (b) The cross-section view of the proposed fingertip.	11
Figure 2. The proposed fingertip was designed and assembled in SolidWorks.	12
Figure 3. The collision model was constructed in the simulator.....	13
Figure 4. The contact states between thin rectangular objects and the planar surface.	14
Figure 5. Simulated stress on fingertip surfaces.	15
Figure 6. MFD distribution inside Finger 1 in case of Point A state.	16
Figure 7. Simulation results of Finger 1 and 2 in terms of sensor outputs. The contact states (Point A, B, and edge) can be classified based on the 3-axis MFD changes.....	17
Figure 8. The fingertip fabrication process: (a) The upper and lower molds were printed using a 3D printer. (b) The liquid silicon rubber was put into the molding cast. (c) The upper and lower molds were attached, and the liquid silicon was left for 24 hours for curing. (d) Four neodymium magnets were embedded inside the soft body. (e) The soft body was fixed to the upper base using a strong adhesive.	19

Figure 9. Two Hall sensors (MLX90393) were fixed on the lower base of the fingertip and the magnet distribution inside the soft body. (b) Isometric view of the fabricated soft fingertip.20

Figure 10. Experimental setup for load and unload test: a thin circuit board was pushed by linear stage in Zs direction with 3 mm of depth displacement. Then, the board was released to the original position for the unload test.21

Figure 11. Hysteresis result in z-axis sensor coordinate.22

Figure 12. Tactile system24

Figure 13. ROS system.26

Figure 14. The graph for visualizing the interaction between nodes and topics constructed in the ROS platform.26

Figure 15. The thin circuit board was grasped by soft fingertips with different orientations.28

Figure 16. (a) The contact position on the fingertip surface. (b) The board made contact at the labeled contact position in the grasping test.29

Figure 17. Neural network architecture to estimate object orientation of thin objects.30

Figure 18. Experimental setup for grasping tasks with different board thicknesses.32

Figure 19. The average error of grasping task with different board thicknesses34

Figure 20. The circuit board made collisions with different contact states38

Figure 21. Neural network architecture to estimate contact state of thin rectangular objects.39

Figure 22. Contact direction movement of the arm for (a) edge contact, and (b) Point A and B contact.42

Figure 23. Experimental setup for contact state estimation.43

Figure 24. (a) Part A was grasped by the gripper. (b) Part A was picked up to the initial insertion position that was approximately 20 mm above Part B.44

Figure 25. The contact state definition: (a) state 0, (b) state 1, (c) state 2, and (d) state 3.44

Figure 26. The range of normal force and Hall sensor data to be input into calibration data sets for (a)–(b) State 1, (c)–(d) State 2, and (e)–(f) State 3.45

Figure 27. Neural network architecture with four hidden layers to estimate (a) contact state and (b) normal force of electrical inverter.46

Figure 28. (a)–(j) Ten trials validation test of State 1 with untrained flange orientation, 15°.....49

Figure 29. Part A was collided to Part B with untrained flange orientation (rotated 15° along y-axis GCS and 5° along x-axis GCS) for (a) state 2 and (b) state 3.50

Figure 30. (a)–(j) Ten trials validation test of State 2 with untrained flange orientation.51

Figure 31. (a)–(j) Ten trials validation test of State 3 with untrained flange orientation.	52
Figure 32. Part A was grasped with untrained grasping position of displaced +5 mm and -5 mm position.	54
Figure 33. (a)–(e) Five trials validation test of State 1 with untrained grasping position +5 mm.	54
Figure 34. Five trials validation test of State 2 with untrained grasping position +5 mm.	55
Figure 35. Five trials validation test of State 3 with untrained grasping position +5 mm.	56
Figure 36. Five trials validation test of State 1 with untrained grasping position -5 mm.	57
Figure 37. Five trials validation test of State 2 with untrained grasping position -5 mm.	58
Figure 38. Five trials validation test of State 3 with untrained grasping position -5 mm.	59
Figure 39. Feedback flowchart.....	61
Figure 40. State 1 feedback using Denso Robot.	62
Figure 41. State 2 of feedback using Denso Robot.....	62
Figure 42. State 3 feedback using Denso Robot	63

Figure 43. Experimental setup: Part A was put on the sponge. Template matching was applied to grasp the part.....64

Figure 44. Three cameras were employed to perform visual feedback. The arm was in State 1.65

Figure 45. State 1 condition using visual feedback for part insertion.....65

Figure 46. State 2 condition using visual feedback for part insertion.....66

Figure 47. State 3 condition using visual feedback for part insertion.....67

List of Tables

Table 1. Specifications of MLX90393.....	24
Table 2. Estimation error of trained contact position and orientation.....	33
Table 3. Estimation error of untrained contact position.....	33
Table 4. Estimation error of untrained contact position and orientation.....	34
Table 5. Training condition for contact states of thin rectangular objects.....	38
Table 6. Classification probability at trained object orientation	40
Table 7. Classification probability at untrained object orientation	41
Table 8. Result of untrained contact directions.....	42
Table 9. Normal force required for the trained FNN to detect the corresponding contact states.	50
Table 10. Normal force required to detect the corresponding contact states with untrained grasping position of +5 mm.	56
Table 11. Normal force required to detect the corresponding contact states with untrained grasping position of -5 mm.	59

CHAPTER 1.

Introduction

Soft robotics has been widely studied in recent years due to its high potential in robotic systems. Researches are inspired by biological creatures in designing soft robotics, such as octopus arms, elephant trunks, and snail feet [1]. Part of soft robots is made from elastic and flexible materials that give such robots an advantage in flexible motion under external forces. It causes soft robots to deal with uncertain and dynamic task environments, compared to conventional rigid-body robots that are more rigid in structure and motion [2]. In particular, due to the mechanical compliance of soft robots, the robots could deform the shape or body structure under unplanned external forces. The advantage is crucial to adapt with the uncertain environments physically. Thus, as the advantage of being soft, such robots could provide passive compliance even without complicated or advanced control systems [3]. Currently, humanoid robots that are developed from flexible materials are intensively studied [4]–[6]. The passive mechanism of the robots could tolerate unpredictable human motion or behavior that benefits in safety environment when interacting with a human. Besides, a soft locomotive robot [7], a bio-inspired soft wearable robot [8], a walking robot with soft joints [9], *etc.*, are other wide applications of soft robots.

On the other hand, the adaptability to react and handle unknown shape of objects is one of the advantages of soft actuators, i.e., soft grippers. In the soft robotics field, many of the soft grippers are pneumatically driven to deform their shape to perform grasping tasks. It can be compliant with various kinds of target grasped objects, as well as able to achieve stable grasping even with a simple control system. By customizing the geometry of the air chambers and the softness of the elastomer, the generated stress from the pressurized air could be change, and the desired gripper's motion is able to be performed. The promising results were demonstrated as the following devices: a prestressed soft gripper for food handling [10], an underwater soft gripper for fragile reefs manipulation [11], a combination of soft and hard materials of soft gripper [12], and others.

Furthermore, equipping a soft gripper with tactile sensation to provide an object's state of feedback as well as recognize other changes in the environment has been receiving much attention to boosting robotics technology. In [13], a soft hand with tactile sensation to grasp a variety of deformable objects was introduced. A soft pneumatic actuator with force feedback to apply a specific pushing force was presented in [14]. Moreover, soft grippers embedded with liquid metal strain sensors [15], and strain sensitive capacitors [16] to provide tactile feedback were proposed. The integration of tactile sensation in the soft robotics field could give a solution in acquiring contact feedback when physically interacted with various kinds of objects. Hence, the closed-loop of the robotic control system can be achieved to automate soft robotics.

1.1 Soft tactile sensors in robotic systems

Tactile sensation contributes to providing essential information on the contacted objects for robotic systems. Applied forces, shapes, material properties, could be acquired by tactile sensors through physical contact with the target objects. In recent years, the soft tactile sensors have been actively studied because of their assuring performance in detecting such modalities at a reasonable cost. The soft tactile sensors cover a broad spectrum of applications, including minimally invasive surgery applications [17], [18], micromanipulation field [19], [20], dexterous robotic hands [21][22], parts assembly [23], and others. The material classification technique based on tactile sensing data was presented [24]–[26].

Magnetic-based tactile sensors have been actively developed in recent years owing to their advantages in detecting contact forces, vibration, material/surface classification, slippage, *etc.* Among these sensors, a mathematical model for a 3-axis force sensor was reported in [27], [28], where changes of magnetic flux density (MFD) was translated into applied normal and tangential force. A design of a pyramid-shaped force sensor using a 3-axis Hall sensor was applied in force-controlled pick and place tasks [29]. A magnetorheological elastomer was used to fabricate a flexible tactile sensor, that is able to solve fractures and poor maintainability issues of soft coverings [30], [31]. Research on texture and slip detection by utilizing magnetic-based tactile sensors were recorded in [32]–[34]. Applications in humanoid robots to precisely detect 3-axis force were described in [35][36]. In addition, a Hall effect-based tactile sensor made of magnetic powder blended with silicon rubber to estimate force without quick saturation is proposed [37]. The

application of magnetic-based tactile sensors was further extended in the development of a robotic skin distributed with Hall sensors for 3-axis force measurement [38], [39].

However, designing a simple structured soft tactile sensor with a minimal number of sensors for assembly tasks is a challenging task. In a situation in which a tactile sensor has to pick and assemble thin PCB boards, the estimation of object orientation and gripping force during grasping tasks is a necessity to achieve successful assembly. Moreover, the tactile sensor needs to grasp in stable condition at the edge of circuit boards since most of the sensitive electric components are placed on the board surface. The recent study on assembling a PCB board using a 6-axis robot was reported in [40], however, the estimation method of object orientation and gripping force of such objects is yet to be discussed. In addition, geometric constraints could occur during part insertion of the assembly task. Thus, the identification of contact states between the grasped objects and the environment is essential. Therefore, in this dissertation, a simple-structured design of the magnetic-based soft tactile sensor, namely soft fingertip, was proposed to estimate the object orientation, gripping force, and contact states of assembly parts, e.g., thin circuit boards, electrical inverter, *etc.* Commonly, in order to estimate the contacted object orientation, more than two Hall-effect sensors were applied, such as in [38], [41], [42]. It causes a higher cost of fabrication as well as a complex structure of soft tactile sensors due to a higher number of embedded Hall sensors. Moreover, the developed magnetic-based soft tactile sensors are commonly dedicated to handling daily objects, such as in [35], [41], [43], whereas the tactile sensors purposely to manipulate assembly parts, e.g., thin circuit boards, electronic parts, and electrical inverters have not been investigated.

The design of the soft tactile sensor has been proposed in our previous work to address such issues [44]. The fingertip design consists of one Hall sensor and five magnets. The experimental tests presented that the orientation of the contacted thin rectangular object, i.e., a thin circuit board, could be determined by a nonlinear relationship from sensor outputs. Then, a geometrical optimization method of the fingertip with same the design was given in [45]. The cylindrical shaped of fingertip was optimized by maximizing magnet displacement, with the two design variables, i.e., hollow radius and magnet position. The optimization framework was performed using Abaqus and Isight, and we found that the optimized design exhibited the least average error compared to other three design candidates. However, the proposed fingertip design has the limitation in sensing area, i.e. the edge of thin objects has to be in contact with the center of the fingertip surface during grasping. Therefore, in this dissertation, a new arrangement of fingertip design is proposed to increase the sensing area. Some results related to the current fingertip performance was given in [46].

In this study, magnetic-based soft tactile sensors are more preferable because of its simple structure and small IC package, compared to other vision-based tactile sensors which often require extra spaces for setting cameras, such as in [47]–[49], and strain gauges that also require more substantial space to fabricate [50]. Thus, small and simple structure of tactile sensors could be achieved, so it is more feasible for the parallel gripper. In addition, shorter sampling time can be achieved by applying Hall-effect based tactile sensors that is up to 1×10^{-6} sec (1 MHz), compared to vision-based tactile sensors that is commonly limited to 0.033 sec (30 fps) of sampling time [51]. In comparison with other tactile sensors that require a much complex fabrication process [19], [52], the fabrication of the fingertip is much simple.

1.2 Modeling of soft tactile fingertip

Modeling of soft fingertips to simulate stress-strain under external force has been performed in past years. The hemispherical-shaped soft finger contact mechanics, commonly used in robotic grasping manipulation, were simulated using finite element analysis [53]. The beam bundle model was introduced to describe the stick and slip event that occurred during the sliding action of soft fingers [54][55]. A human fingertip was modeled to observe the mechanism of human finger sensation [56]. Then, the proxy-based algorithm for simulating contact between one or more fingertips and a virtual object was introduced in [57]. Soft pneumatic fingers were also simulated using a finite element (FE) simulation in [58], and a mathematic model in [12]. However, the above research only addresses soft finger deformation with stress-strain prediction. Instead, in order to simulate magnetic-based tactile sensors output, the MFD distribution induced by the embedded magnets should be simulated. In [27], a mathematical model approach to simulate a simple geometry of a soft tactile sensor with a magnet and a Hall sensor was presented. However, the above method could be difficult to be applied in the condition of the complex geometry of the soft body, as well as multiple magnets and multiple Hall sensors embedded in the soft body. Therefore, in this dissertation, to address such complexity, an FE model of deformation and an FE model of the magnetic field were constructed to simulate the output of the proposed magnetic-based soft tactile fingertip. Based on the simulated magnetic flux density model, the outputs of such tactile sensors could precisely be predicted.

1.3 Contact state estimation in assembly tasks

In assembly parts, i.e., part insertion task, the state of contact between the grasped objects and the environment varies as the operation proceeds. The robotic motion may proceed depends on the contact state that occurred to ensure a successful assembly. Thus, to support the reconstructing of robotic motion strategies, the identification of contact states is essential during the assembly task. The control strategy of manipulators could be constructed by taking into account the contact state estimation method. The contact state estimation of the peg-in-hole task based on force-controlled manipulators was reported in [59]–[62]. The contact state sequence between a robot and the environment was successfully performed using only position sensing [63]. A method to solve the contact state estimation of the large length-diameter ratio peg-in-hole assembly problem was presented in [64]. However, the above research was applied force information, i.e., using Force/Torque sensor to estimate contact state between objects and the environment. The contact state estimation method based on magnetic-based tactile sensor signal output has not been investigated.

1.4 Research objectives

As discussed above, the tactile fingertip with the minimal number of sensors to estimate object orientation, gripping force, and contact state has not been discussed. Thus, the main focus of the research is to develop the tactile fingertip to be applied to robotic parallel gripper for assembly tasks. The objectives of the dissertation are as below:

1. To develop tactile fingertips that can estimate the object orientation and gripping force based on MFD changes during grasping motion.

2. Developing the classification method based on MFD changes to discriminate contact states between the grasped object and the environment.
3. Demonstrating the application of contact state classification method in a feedback system of false insertion detection.

In other words, we hope that our present work is able to help us to apply the tactile fingertips in developing a fully automated robotic assembly system in the future. Besides, possible application fields of the proposed fingertip may include robotic assembly manipulations, aerial robot applications, humanoid robots, rescue robots, and others.

1.5 Dissertation organizations

In Chapter 1, a brief introduction and the literature review related to soft tactile sensors were provided. The objectives of the present work were stated.

In Chapter 2, the principle of the proposed tactile fingertip is described. Then, the design of fingertips with the arrangement of magnets and Hall sensors is given. The constructed finite element model to simulate the fingertip deformation and MFD distribution inside the soft body is presented. The steps to fabricate the fingertip are explained.

In Chapter 3, the system integration applied in the experimental tests was described. The system composed of four Hall sensor chips, a force sensor, a Denso robot, and the Arduino board was integrated into one system.

In Chapter 4, the experimental test to estimate the object orientation of a thin rectangular object, i.e., a thin circuit board, was detailed. The neural network is calibrated by preparing the calibration data sets that consist of Hall sensors output signals with various

trained object orientation. Then, the trained network was validated to estimate the orientation and gripping force of the circuit board.

In Chapter 5, the discrimination method of contact states between the grasped object and the environment based on the proposed tactile fingertip was given. A thin circuit board and an assembly part were chosen to be the manipulated object. The contact states between the grasped object and the environment were defined clearly in this chapter. Then, based on MFD changes, the neural network was trained, and the estimation of the contact state that consists of several tests was performed. Results and discussions on fingertip performance were provided for validation.

Finally, in Chapter 6, the conclusions of this dissertation were described. Furthermore, the suggested direction of future work and applications of the proposed tactile fingertip were presented.

CHAPTER 2.

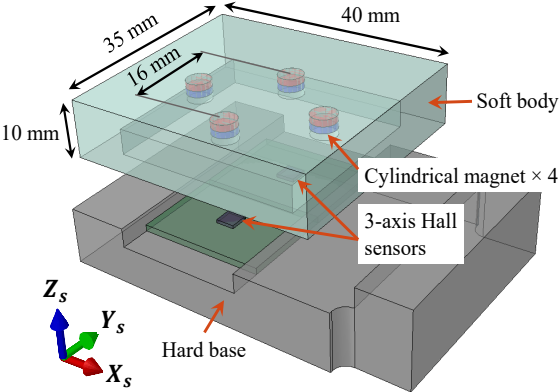
Design and Modeling of Soft Fingertip

2.1 Design principle

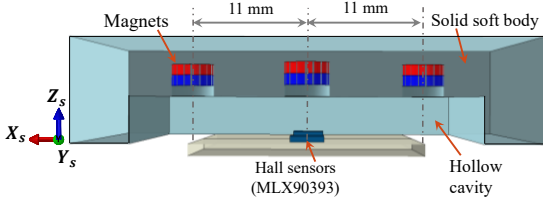
The proposed tactile fingertip consists of two Hall sensors that were arranged in parallel and fixed to the solid base of the fingertip, as shown in Figure 1. Four cylindrical magnets were embedded with square pattern distribution in the soft rectangular body. The rectangular shape of the soft body was preferable because the contact area for grasping objects could be maximized, unlike the cylindrical shape of the previously suggested design [27]. As a result, stable gripping could be generated, and also beneficial to modeling and analysis. A hollow cavity was introduced in the design to let the soft body cope with the large deformation during assembly tasks. The fingertip was designed and assembled in SolidWorks as illustrated in Figure 2.

When an object was contacted to the fingertip surface, the soft body will be compressed and deformed. The magnets embedded inside the fingertip will be displaced. The displacement of the magnets caused changes in the magnetic field near the Hall sensors. Therefore, by analyzing the changes in magnetic flux density induced by the magnets, the object orientation of the grasped object could be estimated. Similarly, when the fingertips

grasped the assembly parts and made contact with several predefined contact states, the changes of MFD induced by the magnets are produced. By detecting the changes of MFD, the contact states could be determined. Finally, a machine learning approach of the neural network was constructed to clarify the relationship between MFD changes and the corresponding object orientation, gripping force, and contact state.



(a)



(b)

Figure 1. Arrangement of magnets and Hall sensors in the exploded view. (b) The cross-section view of the proposed fingertip.

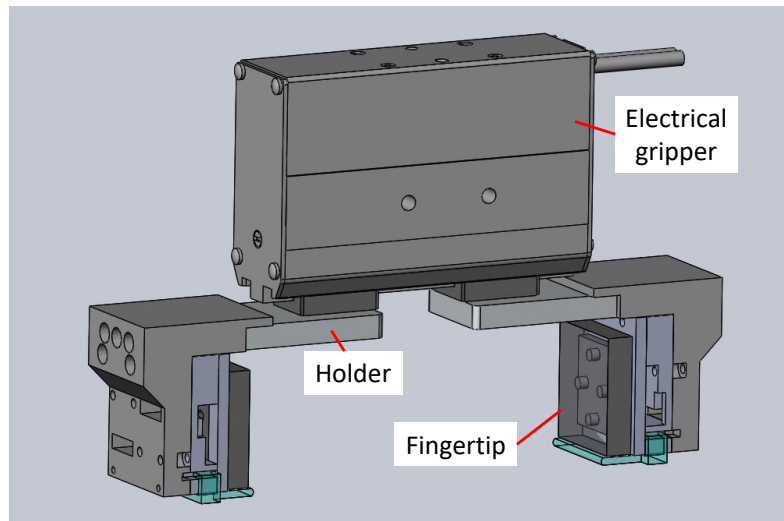


Figure 2. The proposed fingertip was designed and assembled in SolidWorks.

2.2 Finite element simulation

The finite element simulation was carried out to investigate the applicability of the proposed fingertip with a given arrangement of the magnets and Hall sensors for categorizing contact states. A thin rectangular object was grasped by a pair of fingertips and made contacts with an environment, i.e., plane surface. To evaluate the design, the distribution of the simulated MFD was observed by considering different contact state collisions. The design of the fingertip is assumed to have enough features if the MFD changes are not distributed in the single concentrated spot for different contact states. FE models of deformation were constructed to simulate the geometrical changes during a collision. Then, FE models of electromagnetic analysis were constructed for simulating MFD distribution that is induced by the magnets. Both simulation steps were performed using Abaqus (Dassault System, Waltham, MA, U.S.) with a Windows operating system of 32GB memory.

2.2.1 Simulating deformation

The collision model constructed in Abaqus is shown in Figure 3. A plane surface was placed horizontally in the x-y plane. The thin rectangular object was positioned between two fingertips. P_1 and P_2 denote the center of the fingertip surface for each finger. In the setup, the board made contact with P_1 and P_2 . The distance values of d_ξ and d_ζ were set as 17.5 mm and 20 mm, respectively. The angle of Φ is defined as the angle between the board-side and the plane surface. Meanwhile, the angle of ψ is given by the acute angle of the board end to the plane surface.

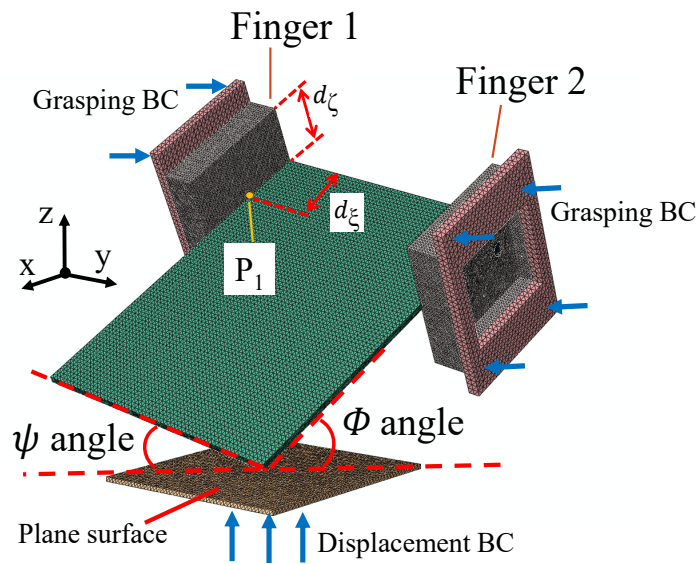


Figure 3. The collision model was constructed in the simulator.

The contact states' definition between thin rectangular objects and the plane surface as the environment is described in Figure 4. Point A state is defined as the right tip of the board-end collides with the plane surface. Point B is described as the left tip of the board-end

made contact with a plane surface. On the other hand, the edge state is defined as when the edge of the board-end collides with the plane surface, i.e., the angle of ψ is 0° .

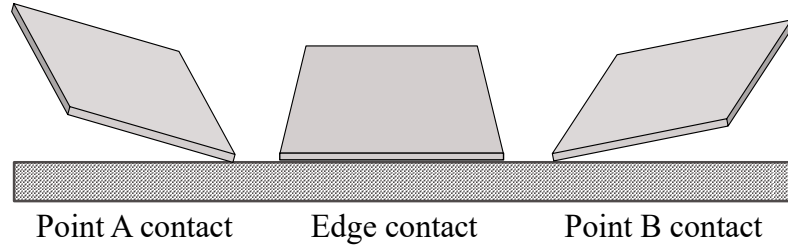


Figure 4. The contact states between thin rectangular objects and the planar surface.

In the simulator, the soft body, and hard material (thin board, magnets, hard base, plane surface) were set as linear elastic materials. In this simulation, the soft body of the fingertip was assumed to be fabricated by a 3D printer. Therefore, Young's modulus was set to be 0.59 MPa and 2000 MPa to simulate the material properties of the TangoPlus and VeroWhite materials of a 3D printer, respectively. The Shore hardness to Young's modulus conversion was previously calculated in [10]. The Poisson's ratio was set to 0.48 for the soft material, and 0.3 for the hard material. Based on the TangoPlus material's datasheet, the density of the soft body was set as 1120 kg/m^3 . To simulate the connection between different materials, 'tie' constraints were selected in Abaqus. In addition, the interaction between the soft body and board, and the board and the plane, were specified as tangential and normal behavior by utilizing a penalty method, that is available in Abaqus's setting. A friction coefficient was set to 0.7. All parts have meshed with 4-node tetrahedron elements.

To perform the simulation of the collision, two steps were conducted: a grasping step and a collision step. In the grasping step, the grasping displacement of boundary condition (BC) was applied to grip the board for 1 mm dept. Next, in the collision step, two BCs were

defined: (1) both fingertip bases were fixed in space, and (2) the displacement BC was applied to the plane surface considering collision motion in z-axis for 1 mm. For Point A and B states, the angle of Φ was set as 30° , and the angle of ψ was set as 10° , 20° , and 30° . In the edge contact state, the angle of Φ was set to 10° , 20° , and 30° .

Figure 5 presents the stress distribution of the simulation result for Finger 1 and 2, in the case of Point A state. The light color represents higher stress distribution. It can be observed that the higher stress has occurred at the middle of the fingertip surface, i.e., contacted location. Furthermore, it can be understood that the deformation effects of Fingers 1 and 2 were different after the collision step of Point A or B state. This resulted in different MFD changes for both fingers.

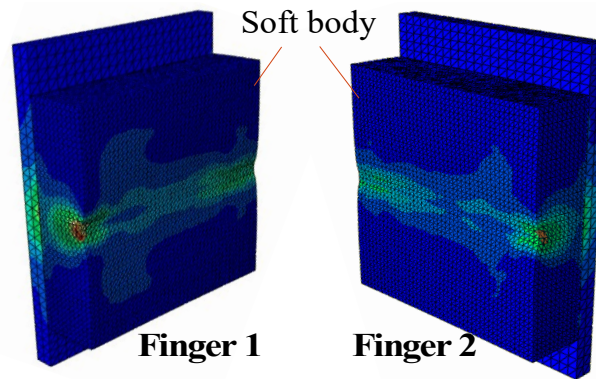


Figure 5. Simulated stress on fingertip surfaces.

2.2.2 Magnetic field simulation

To simulate the MFD distribution induced by Hall sensors, the FE model of magnetic field simulation was performed. Initially, in an Abaqus model of FE electromagnetic analysis, the deformed geometries and positions of four magnets and two Hall sensors from the FE model of deformation were imported as orphan meshes. Then, to simulate the outer air domain, a

cylindrical shape (50 mm × 40 mm) was created in the model. Next, all geometries (air domain, magnets, Hall sensors) were merged by retaining the intersecting boundaries between different partitions. After partitioning each part of the magnet, Hall sensor, and air domain, the magnetic properties of permeability were modeled as $4\pi \times 10^{-7}$ H/m. Then, the direction of the magnetic field (from south to the north pole) was appointed for each magnet, with the magnetic coercivity of 955 kA/m, as to model the magnetic characteristic of the applied neodymium magnet. Then, at the outer surface of the air domain, the BC was applied to initiated magnetic vector potential on the boundary surface. The constructed model was meshed with the 4-node linear tetrahedron electromagnetic element. The simulation was repeated for each condition with different contact states. As a result, the distribution of MFD in the case of Point A state after the collision is shown in Figure 6. The bright color represents the north pole of the magnet.

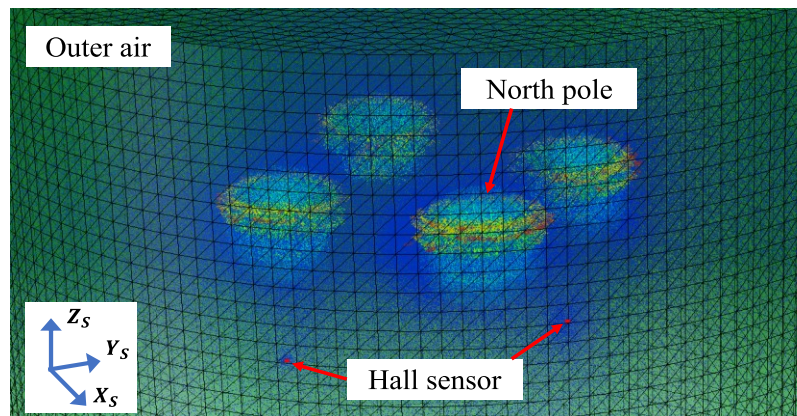


Figure 6. MFD distribution inside Finger 1 in case of Point A state.

2.2.3 Simulation results

The MFD changes of different contact states were plotted and shown in Figure 7. Based on the graph, the values of MFD changes are distributed clearly in three separate regions for three different contact states that can be represented by dotted rectangles. Thus, it can be noted that the proposed design of tactile fingertip was successfully able to classify contact states between the grasped object and the environment.

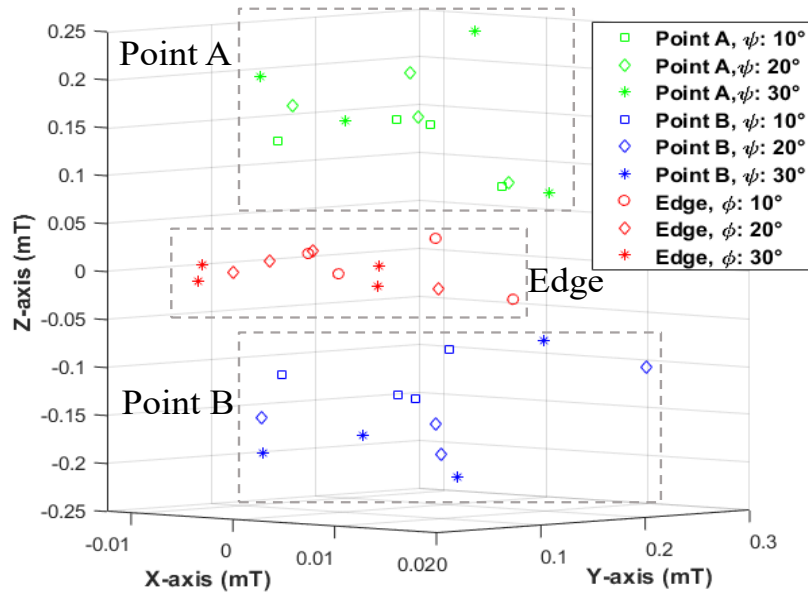


Figure 7. Simulation results of Finger 1 and 2 in terms of sensor outputs. The contact states (Point A, B, and edge) can be classified based on the 3-axis MFD changes.

2.3 Fabrication of soft fingertip

The fingertip was fabricated with the same geometry given in Section 2.2. The soft body of the fingertip was made of soft silicon rubber (Dragon Skin 20, Smooth-On, U.S.) [65]. First, to make the soft body, the upper and lower mold (Figure 8(a)) was printed using a 3D printer

(M200, Zortrax, Poland). The molds were designed in SolidWorks based on the shape of the fingertip. Then, the liquid silicone rubber of Dragon Skin 20 was poured into the lower molding cast, as shown in Figure 8(b). The mold was placed in a vacuum chamber with a pressure of 0.1 MPa to remove air bubbles that mixed in the liquid silicon. Both upper and lower molds were attached with screws (Figure 8(c)) and were left for curing. The cured soft body was removed from the mold. Four neodymium magnets were embedded inside the soft body using a strong adhesive, as given in Figure 8(d). The magnets were arranged so that the south pole of the magnets faces the chips. In this study, the magnets manufactured by Magfine Co. Ltd., Japan [66] with a size of 4 mm in diameter and 2 mm in height, are used. In particular, the magnet has the characteristic of a surface magnetic flux density of 3300 Gauss. Then, the soft body was glued to the upper base.

Next, two chips of Hall sensor (MLX90393, Melexis Co. Ltd.) were fixed in parallel to the lower base of the fingertip, as shown in Figure 9(a). The upper and lower base of the fingertip was 3D-printed using Connex3 Objet350 Printer with VeroWhite material. The fabricated tactile fingertip is presented in Figure 9(b).

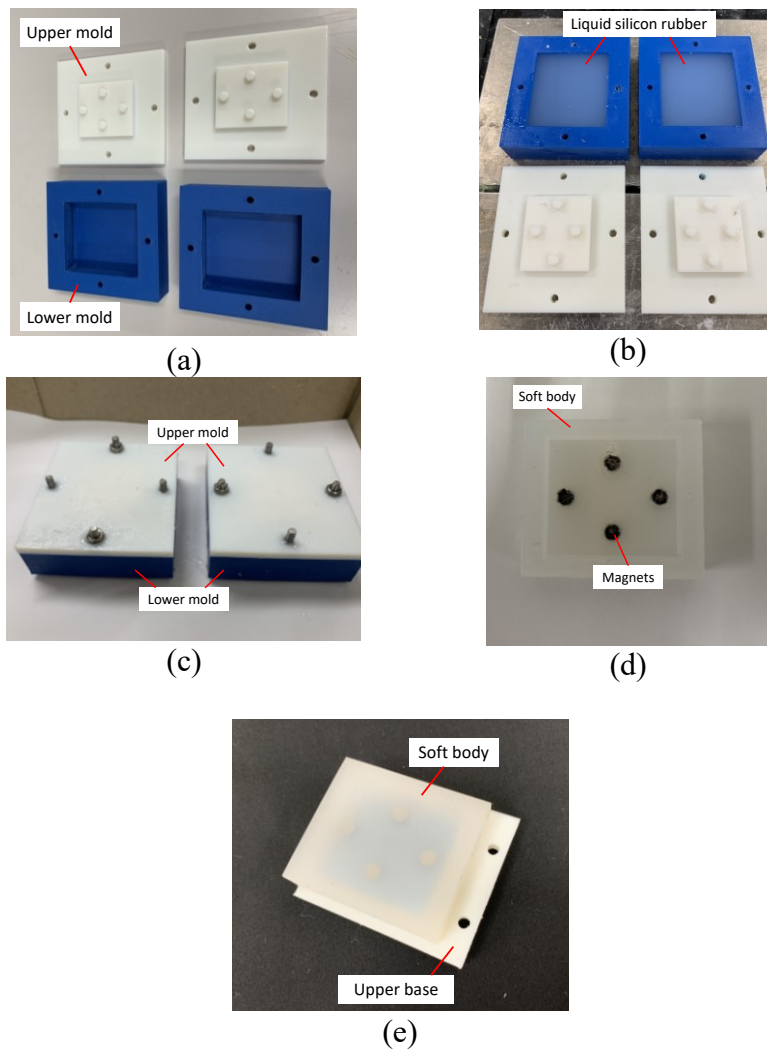
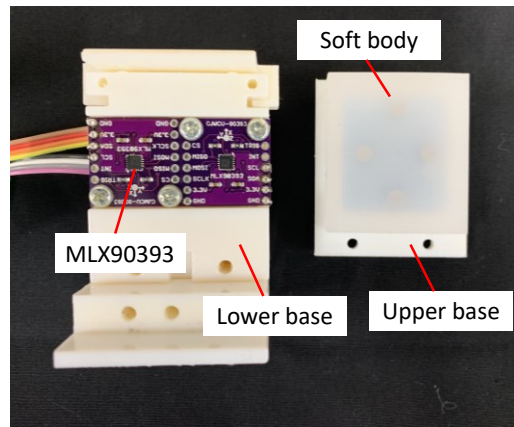
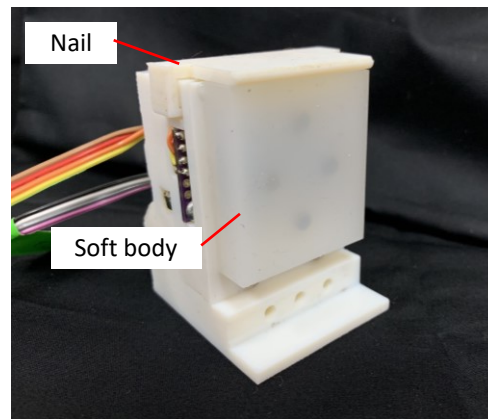


Figure 8. The fingertip fabrication process: (a) The upper and lower molds were printed using a 3D printer. (b) The liquid silicon rubber was put into the molding cast. (c) The upper and lower molds were attached, and the liquid silicon was left for 24 hours for curing. (d) Four neodymium magnets were embedded inside the soft body. (e) The soft body was fixed to the upper base using a strong adhesive.



(a)



(b)

Figure 9. Two Hall sensors (MLX90393) were fixed on the lower base of the fingertip and the magnet distribution inside the soft body. (b) Isometric view of the fabricated soft fingertip.

2.4 Hysteresis test

The hysteresis characteristic of the fingertip was evaluated with load and unload tests, as shown in Figure 10. In the test, a thin circuit board was load and unload onto the fingertip surface in the normal direction (z-axis). The fingertip was mounted on a load cell for recording normal force measurements. The circuit board was moved vertically with 1 mm/s of velocity for the displacement depth of 3 mm from the fingertip surface. The normal force

and the z-axis MFD from one of the Hall sensors were measured as the loading data set during pushing motion. The circuit board was released to the original position after 3 sec rest. Both tests were conducted at a sampling frequency of 50 Hz. The hysteresis value (%) was calculated as the following equation:

$$Hysteresis = \left| \frac{(Z_{smu} - Z_{sml})}{(Z_{smax} - Z_{smin})} \right| \times 100, \quad \text{Eq. 1}$$

where Z_{smax} and Z_{smin} indicate the maximum and minimum of the measured z-axis MFD respectively. The measured z-axis MFD at the midpoint between the minimum and maximum of the normal force value was presented by Z_{smu} and Z_{sml} . The graph in Figure 11 describes the hysteresis property of the sensor. It can be observed that the hysteresis was 7.3% of the full scale. Hysteresis occurs owing to the soft material characteristic that resulting in a nonlinear relationship between normal force and sensor output.

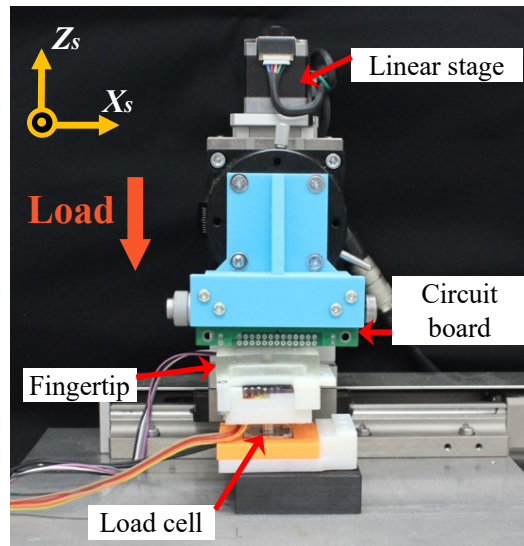


Figure 10. Experimental setup for load and unload test: a thin circuit board was pushed by linear stage in Z_s direction with 3 mm of depth displacement. Then, the board was released to the original position for the unload test.

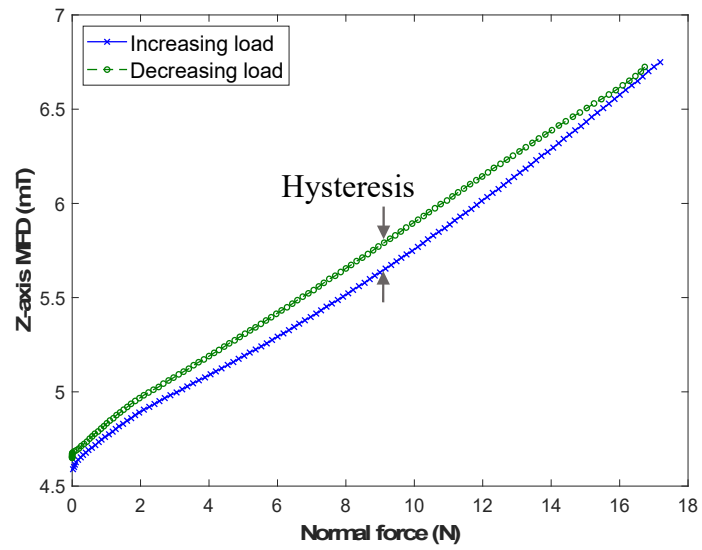


Figure 11. Hysteresis result in z-axis sensor coordinate.

CHAPTER 3.

System Configuration and Equipment

3.1 Introduction

In this chapter, the system configuration to integrate all electronic components for performing validation tests is given. The tactile system is employed to acquire Hall sensor signals and 3-axis force data. Then, the neural network to define the relationship between sensor signals to the object orientation, contact states, and contact force is given. The feedback control system consists of a tactile system, and a 6-axis robot is given.

We applied Robot Operating System (ROS), an open-source middleware operating system to synchronize all components. It provides libraries and tools that can be integrated with various sensors, cameras, robots, *etc* [67]. Several programs, i.e., nodes, can be created in a ROS environment, and a ROS Master is applied to manage messages that are transmitted between nodes for communication.

3.2 Tactile system

The tactile system applied in this study is shown in Figure 12. Four 3-axis Hall-effect sensors (MLX90393, Melexis Co. Ltd.), as given in [68], with total of 12 output signals, were employed to measure MFD changes during assembly tasks. The specification of the Hall

sensor is presented in Table 1. The sensors were connected to I2C multiplexer (TCA9548A, Texas Instruments Co. Ltd.) by I2C communication protocol to synchronize the measurements simultaneously. The measurement frequency was set to 50 Hz. Then, an Arduino Uno was used to record Hall sensors measurements. SDA, SCL, 3.3 V and GND ports were connected between the multiplexer and Arduino. Furthermore, a 3-axis force sensor (PFS055YA251U6, Leptrino Co. Ltd., Japan) was employed as a reference sensor and was linked to a computer. Finally, the MFD measurements and 3-axis forces were synchronized in the ROS platform.

Table 1. Specifications of MLX90393

Specification	Detail
Signal size	16-bit output for all 3-axis (x,y,z)
Measurement range	5–50 mT
Sampling rate	500 Hz
Available communication	I2C or SPI protocol

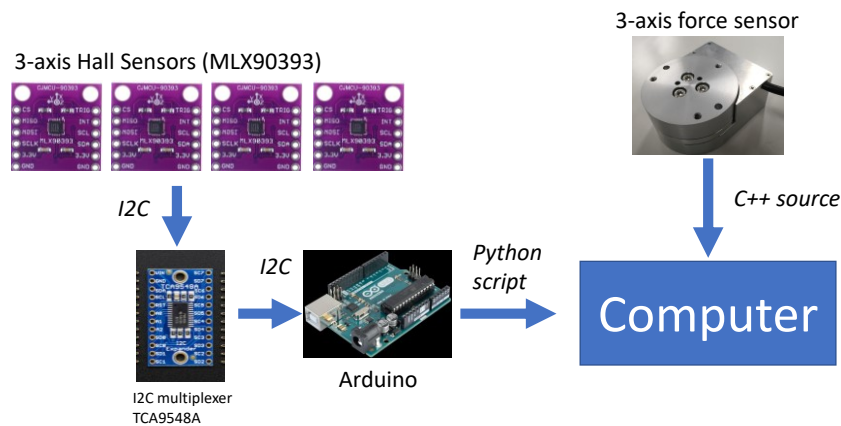


Figure 12. Tactile system

3.3 Feedback control system

Figure 13 shows the configuration of the feedback control system, where Hall sensors, an Arduino Uno, a 3-axis force sensor, and a 6-axis Denso Robot (VP-6242, Denso Wave Co. Ltd., Japan) were synchronized simultaneously in ROS platform. We applied ROS Kinetic (2016 release) on Ubuntu 16.04 (Xenial) operating system to perform the feedback system. In addition, ROS package of Denso Robot (Version 1.0.0) was installed in the computer to manipulate the arm. The “*moveit_commander*” Python package was employed to interface Denso Robot for motion planning and execution. In ROS system, a topic name of */haptic* was published from Arduino to ROS Master (computer) to send messages that contain 12 sensor signals, estimated normal contact force, and estimated contact states. A topic name of */force_torque* was published from the 3-axis force sensor to ROS Master to send the information of the measured contact forces. In addition, a node, *read_node* was initiated to publish */read* topic that contains Hall sensor signals, measured normal force, estimated contact state, and estimated normal contact force for plotting. The graph was presented in Figure 14 to visualize the interaction between initiated nodes and topics in ROS platform.

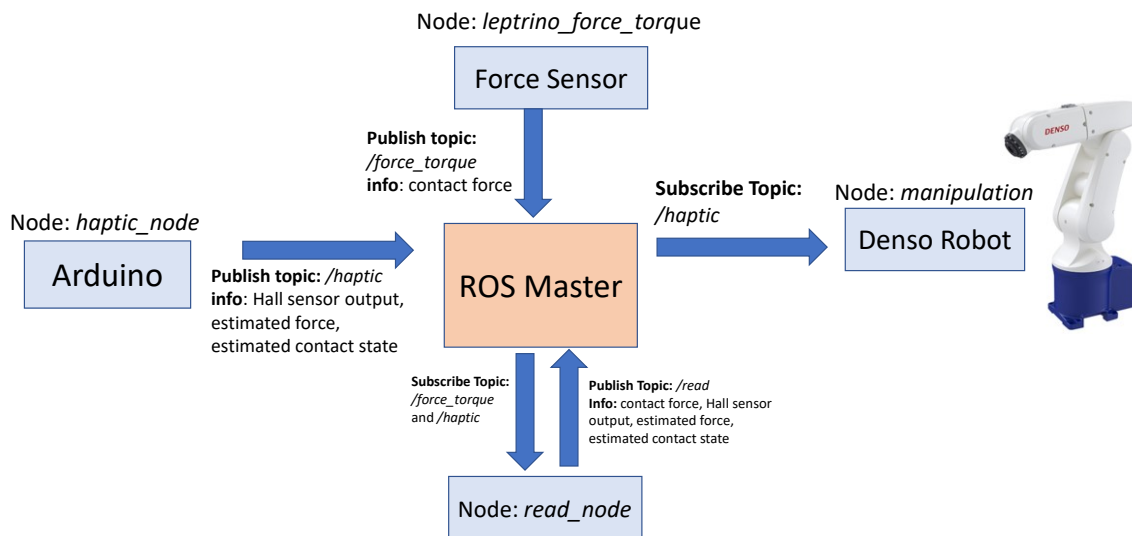


Figure 13. ROS system.

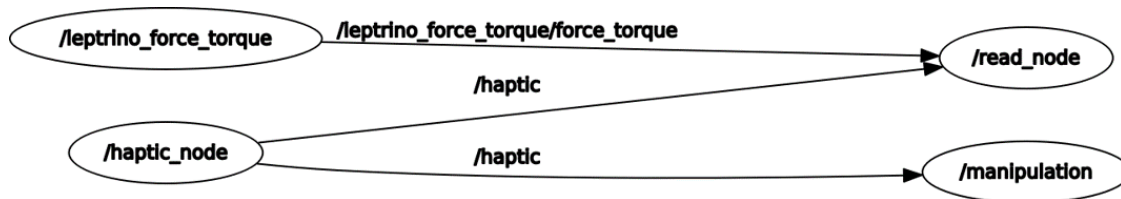


Figure 14. The graph for visualizing the interaction between nodes and topics constructed in the ROS platform.

CHAPTER 4.

Experimental Test of Object Orientation and Gripping Force Estimation

The tactile fingertip was fabricated using the same parameters, as given in Section 2.3. Then, it was verified through FE simulation and experimental tests. In this chapter, the proposed fingertip was tested to estimate the object orientation and gripping force of thin rectangular circuit boards. The calibration method to map MFD changes of sensor signals to object orientation and gripping force was given. Then, the performance of the fingertip in estimating object orientation and gripping force was given in results. The current design limitation will be discussed in the discussion section.

4.1 Calibration procedure

The objective of the calibration procedure is to train the neural network in order to estimate the object orientation and gripping force. In this test, an electrical linear gripper (LEHF20K2-48-R16N, SMC Co. Ltd., Japan) was applied to grip an object. The gripper was connected to the computer and manually controlled by a software (SMC Actuator Software, SMC Co. Ltd., Japan). The proposed fingertip with Hall sensors was attached to one finger of the gripper, as shown in Figure 15. On the finger, the fingertip (with the same geometry) without embedded with Hall sensors was mounted onto a 1-axis load cell (USL6-H5-50N, Tec Gihan,

Kyoto, Japan) for collecting gripping force measurements. The gripper was attached to 6-axis Denso Robot. To synchronize all output data, the Hall sensors and load cell were connected to Arduino Uno, which was linked to a computer. In this test, a thin rectangular PCB board with a size of $120\text{ mm} \times 80\text{ mm} \times 1.7\text{ mm}$ was employed as the manipulated object. The board was placed on the manual rotary stage, which can be rotated manually along y-axis GCS. The stage was put on the horizontal plane. The angle of the board surface to the fingertip surface was assumed to be right angled during grasping tasks. The grasped object orientation is defined as φ angle, and it can be adjusted by rotating the rotary stage manually.

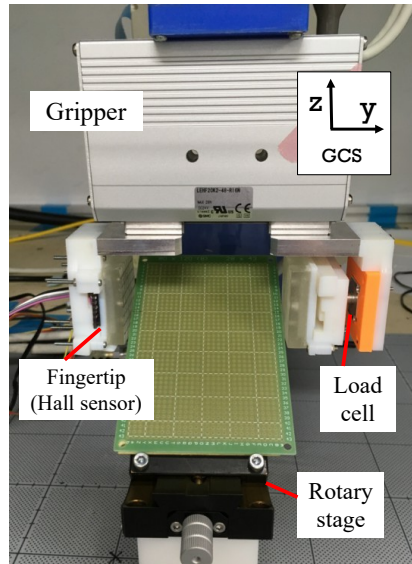


Figure 15. The thin circuit board was grasped by soft fingertips with different orientations.

In this experimental test, 49 contact positions (r, h) on the fingertip surface were defined as the intersection of vertical and horizontal blue dot lines, as illustrated in Figure 16(a). In the calibration procedure, the circuit board was grasped at the given contact positions. The fingertip was manipulated by a robotic arm, such that the circuit board made

contact at the fingertip surface and contacted the target positions with a given φ angle as shown in Figure 16(b). At each contact position, the grasping task was set up with different orientations of φ angle: 0° , 10° , 20° , and 30° . The grasping displacement of 4 mm was applied for each grasping. Ten trials of grasping calibration were performed for each orientation at a predefined contact position. Thus, forty trials of grasping calibration were conducted for each contact position. Hall sensor measurements and force data were recorded for each trial.

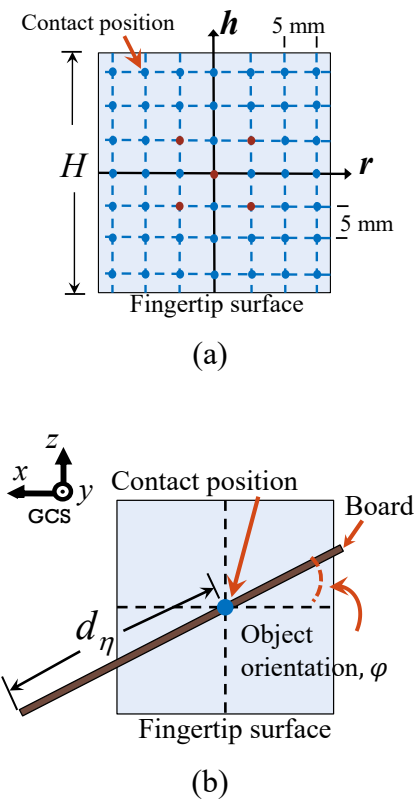


Figure 16. (a) The contact position on the fingertip surface. (b) The board made contact at the labeled contact position in the grasping test.

We applied a machine learning technique to perform the calibration process. A feedforward neural network (FNN) was constructed by using MATLAB Neural Network Toolbox to find the relationship between Hall sensors output and the object orientation and

gripping force. Figure 17 shows the network architecture of FNN to estimate object orientation. The changes of MFD recorded by Hall sensors were taken as inputs (6 signals), and the object orientation and gripping force were taken as target outputs. The network parameters were trained with a hidden layer consisting of twenty neurons. The tan-sigmoid function was applied as the activation function in each neuron. In the output layer, by summing the neuron outputs, A linear transfer function was employed for estimating the output. FNN output is denoted by y_{out} and is defined as follows:

$$y_{out} = \sum_{i=1}^n w_i^{(2)} \sigma \left(\sum_{j=1}^m w_{i,j}^{(1)} x_j + b_{i,j}^{(1)} \right) + b_i^{(2)}, \quad \text{Eq. 2}$$

where m and n denote the number of inputs and neurons, respectively. The variable of w_i is the hidden layer weights and $w_{i,j}$ is the input layer weights. The biases of the network are denoted by b_i and $b_{i,j}$. Besides, σ is the activation function of the hidden layer. In total, the calibration parameters of the trained network were 160 weights (120 input weights, 40 layer weights) and 22 biases. In addition, the Levenberg-Marquardt backpropagation was utilized for optimizing the weights and biases in the network.

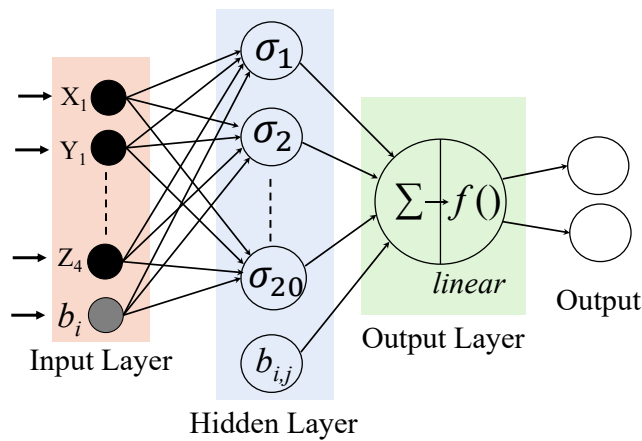


Figure 17. Neural network architecture to estimate object orientation of thin objects.

4.2 Validation tests

A trained FNN was employed to make estimations of the object orientation and gripping force. In validation tests, four tests were conducted: (1) with the condition of both trained contact position and trained object orientation, (2) untrained contact position and trained object orientation, (3) both untrained contact position and object orientation, and (4) different thicknesses of the board.

In the first test, the untrained data series of MFD changes at the trained contact position and object orientation were used as the input of FNN. Five grasping trials were repeated at random trained contact position for each object orientation. In the second test, for each object orientation, five grasping trials were carried out at random untrained contact positions on the fingertip surface. In the third test, the grasping tests were performed at untrained random contact position with five trials for each untrained object orientation: 5° , 15° , and 25° . Finally, in the fourth test, the grasping test with different board thickness values was performed to investigate performance in terms of estimating the object orientation with different board dimensions. The experimental setup is shown in Figure 18. Four rigid acrylic boards with different thicknesses of 1 mm, 2 mm, 4 mm, and 8 mm were used. The test was organized considering trained and untrained object orientations. The grasping test was conducted with object orientation of 0° , 10° , 20° , and 30° . At each orientation, 15 trials of grasping tests were conducted with ten trials for calibration input data and five trials for verification data. Then, the verification of which the grasping test was conducted with untrained object orientation of 5° , 15° , and 25° . Five grasping trials were conducted for each orientation.

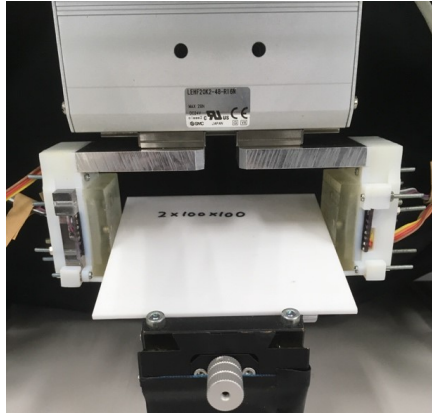


Figure 18. Experimental setup for grasping tasks with different board thicknesses.

4.3 Results and discussion

The result of the first test is shown in Table 2. The average error of object orientation, φ and gripping force, F_g were given in the table. Overall, the average error for all object orientation was 1.96° , which is within 5° . Based on the result, the average error of the gripping force also shows acceptable performance with the average error less than 0.5 N. This proves that the proposed tactile fingertip is able to provide an excellent solution to clarify the relationship between MFD changes of Hall sensor output and the network output, e.g., object orientation and gripping force.

Table 2. Estimation error of trained contact position and orientation

Average error	Object orientation, φ			
	0°	10°	20°	30°
$ \Delta\varphi $ (°)	2.07	2.22	1.92	1.62
$ \Delta F_g $ (N)	0.07	0.11	0.06	0.12

The evaluation result of the second test is listed in Table 3. The result shows that the average error for twenty trials of all orientations was 2.61°. It indicated that even when grasping was performed at the untrained contact position, the trained FNN was still capable of estimating the object orientation with an error of less than 5°.

Table 3. Estimation error of untrained contact position

Average error	Object orientation, φ			
	0°	10°	20°	30°
$ \Delta\varphi $ (°)	3.01	2.55	3.02	1.86
$ \Delta F_g $ (N)	1.84	0.34	0.57	0.58

Table 4 gives the estimation results for the third test of each object orientation. Based on the average result, the overall average error of orientation was 2.00°, which was still less than the range of 5°. Despite the total average error, the gripping force was 1.08 N, slightly larger compared to the first and second tests. However, it was still within the threshold range of 1.5 N. In addition, the larger errors occurred around smaller orientation angles, which were close to 0° was observed. We assumed that the increase in error was due to the least features of MFD occurred while grasping in this orientation. It can be explained that the Hall sensors were arranged in the GCS x -axis (0° of orientation). As a possible solution, the number of grasping calibration trials should be increased for smaller orientation conditions.

Table 4. Estimation error of untrained contact position and orientation

Average error	Object orientation, φ		
	5°	15°	25°
$ \Delta\varphi $ (°)	3.36	1.75	0.88
$ \Delta F_g $ (N)	2.37	0.53	0.35

The result of the grasping test of the fourth test is shown in Figure 19. It can be observed that the estimation error was slightly increased with the increase in board thickness. However, overall, the average error of each thickness is within the range of 5°. Therefore, to address the limitation regarding the object thickness, we assume that the thickness of the grasped object is within 10% of the minimum width of the sensor surface. In this study, since the minimum width of the sensor surface is 35 mm, the thickness of the object is supposed to be below 3.5 mm in order for the fingertip to estimate object orientation in a good performance.

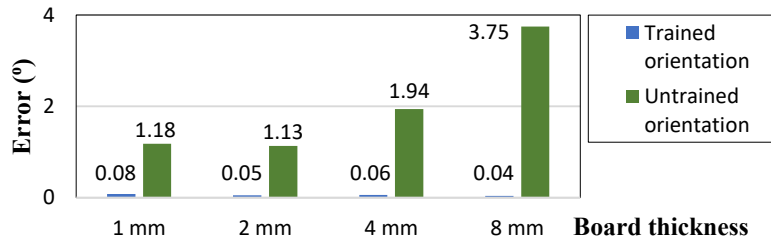


Figure 19. The average error of grasping task with different board thicknesses

In this dissertation, the grasping task was performed with multiple contact positions on the fingertip surface. It shows that the current design has contributed to the increasing in sensing area compared to the previous design in [44], which was limited to only the center of the fingertip. This is because, by supplementing an additional Hall sensor, the input of the

network was increased from 6 signals in the past design to 12 signals. Consequently, the FNN could have enough features to estimate the target outputs, even with various contact positions. In addition, through grasping task at the untrained contact positions in the third test, we validated the robustness of the sensor performance in estimating the object orientation.

CHAPTER 5.

Classification of Contact State

In this chapter, the calibration method is proposed to map MFD to contact states. Then, the fabricated fingertip was evaluated to discriminate the contact states of the grasped objects, e.g., thin circuit boards and electrical inverters. Furthermore, a false insertion detection in the assembly task is given based on Hall sensor output. Denso Robot and Mitsubishi Electric Robot were employed to perform the manipulation.

5.1 Thin rectangular object

The thin rectangular PCB board (Section 4.1) was applied as the manipulated object. In this section, the contact state between the board and the environment (planar surface) is estimated by the fabricated fingertip.

5.1.1 Calibration procedure

The setup for discrimination of contact state test with a thin PCB board is shown in Figure 20. In this test, both fingers were mounted with Hall sensors. Thus, in total, twelve input signals were taken as input to FNN for estimating the contact states. Based on Figure 16(b), the distance of d_η must satisfy Eq. 3 in order to make sure the board makes contact with the plane surface.

$$d_n > \frac{H}{2 \sin \varphi} \quad \text{Eq. 3}$$

In the equation, H represents the length of the fingertip Figure 16(a). Initially, the PCB board was put on the manual rotary stage, which was fixed on the ground. By rotating stage around y -axis GCS, the object orientation, φ could be adjusted to perform the test. The arm was moved towards the stage for grasping. In the software of the gripper, the given grasping displacement of 4 mm was applied, with the gripping velocity of 5 mm/s. At this point, MFD was measured, and the measurements were taken as the initial value. To perform collision onto the planar surface, the arm was moved to a position where the tip of the board was approximately 15 mm vertically away from the environment (planar surface). The acute angle of the board end to y -axis GCS is defined as ψ angle, and it was given by rotating the arm along x -axis GCS. The board contacted the planar surface in z -direction movement, with a collision depth of 3 mm. The MFD values were recorded with a measurement frequency of 20 Hz. To remove offsets, the initial values were subtracted from the MFD values recorded. The board was collided with three different contact states: Point A, Point B, and the edge state. Eight trials were repeated for each condition of collision. Five data sets were taken for the calibration data set, and the remaining three data sets were used for the validation test. The above procedures were performed for different object orientation of 10° , 20° , and 30° . Table 5 shows the overall training condition for contact state estimation of thin rectangular objects (PCB board). As the improvement of the previous design, the contact state discrimination test were conducted with multiple selected contact positions on the fingertip surface. The five contact positions were the center point (0, 0) and other 4 points: (5, 5), (-5,

5), (-5, -5), and (5, -5) represented by red dots in Figure 16(a). Thus, in total, 525 trials of collision tasks were performed.

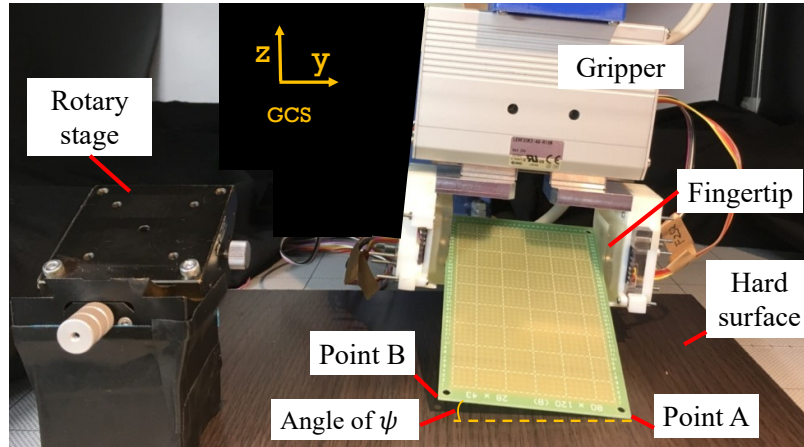


Figure 20. The circuit board made collisions with different contact states

Table 5. Training condition for contact states of thin rectangular objects

Object orientation, φ	Angle ψ	Contact state	Trials
10°, 20°, and 30°	0°	Edge	5
	5°	Point A	5
		Point B	5
	10°	Point A	5
		Point B	5
	15°	Point A	5
		Point B	5

An FNN with one hidden layer and one output layer was constructed to classify the contact states of three predefined classes: Point A, B, and the edge. MATLAB’s Neural Network Toolbox was applied in constructing the network. The network architecture is shown in Figure 21. The input of the network consists of twelve input signals (MFD changes), and the target output is the contact state probabilities, with the values from 0 or 1. In

architecture, the hidden layer is formed by ten neurons. The tan-sigmoid transfer function was applied as the activation function in the hidden layer. The Softmax function is operated as the transfer function for classifying the contact states into categorical probability distribution in the output layer. The backpropagation was performed using the scaled conjugate gradient, and the iteration was limited to 1000 steps during the network training process. The weight and biases of each layer were computed in MATLAB.

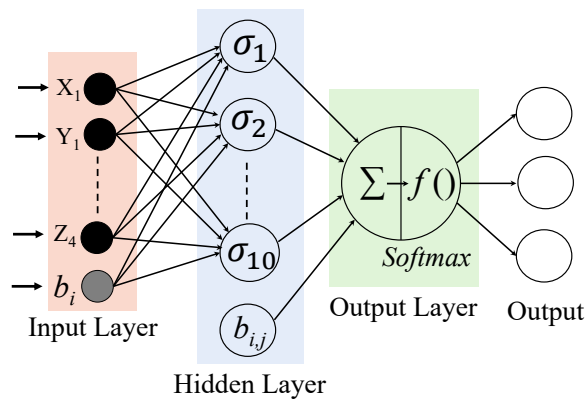


Figure 21. Neural network architecture to estimate contact state of thin rectangular objects.

5.1.2 Assessment tests

Three assessment tests were conducted to validate the performance of the trained FNN with:

- (a) the condition of both trained object orientation and the angle of ψ ;
- (b) the condition of both untrained object orientation and the angle of ψ ;
- (c) the condition of untrained contact direction movement.

(a) The condition of both trained object orientation and the angle of ψ .

In the first test, the inputs were the untrained datasets at the trained board orientations of φ : 10° , 20° , and 30° ; and ψ : 0° , 5° , 10° , and 15° . In total, 135 datasets for Point A and B, each, and 45 data sets for the edge state were used for assessment. Table 6 presents the

classification probability result. The probability is ranging between 0~1, with value 1 indicating the probability of correctly classified input. Based on the estimated average error of each object orientation, it can be observed that the trained FNN can successfully discriminate Point A, B, and edge contact states.

Table 6. Classification probability at trained object orientation

Classification result	Object orientation, φ		
	10°	20°	30°
Point A	1.0000	1.0000	1.0000
Point B	1.0000	1.0000	1.0000
Edge	1.0000	1.0000	1.0000
Average	1.0000	1.0000	1.0000

(b) The condition of both untrained object orientation and the angle of ψ .

In the second test, the contact state classification was performed in the condition of φ , and ψ angles were different from the calibration condition. The evaluation was performed to ensure the robustness of the trained neural network to make classification even in untrained condition. The board was rotated to the untrained object orientation, φ : 15°, 25°, and 35°; and each orientation was tested with angle ψ : 0°, 7°, 12°, 17°. Then, the above evaluation test was repeated for all five contact positions, where three trials were carried out for each condition. In total, 135 data sets of inputs for Point A and B, and 45 data sets for the edge state were prepared. Table 7 presents the classification result. It can be noted that the classification probabilities were all over 90%, proving that the trained FNN was able to estimate the contact states of a PCB board even with the untrained condition of φ and ψ angle.

Table 7. Classification probability at untrained object orientation

Classification result	Object orientation, φ		
	15°	25°	35°
Point A	1.0000	1.0000	1.0000
Point B	0.9778	1.0000	1.0000
Edge	1.0000	0.9286	1.0000
Average	0.9885	0.9898	1.0000

(c) The condition of untrained contact direction movement.

In the third test, the network was evaluated with the untrained contact direction movement. This is because, in real assembly task, the arm may perform movements in multiple axes simultaneously to accomplish the assembly. For edge contact, the board was collided with the hard plane in the incline angle direction 45° and 60° (x and z-axis), as shown in Figure 22(a). Then, the board made contact with a hard plane in the 3-axis inclined angle direction of 45° and 60° for Point A and B contact, as given in Figure 22(b). The contact depth of 3 mm in the z-axis was conducted for each trial. The object orientation, φ , was set to 20°, and the contact trials were repeated for ψ angle of 0°, 5°, 10°, and 15°. Table 8 gives the result of collision trials with untrained contact direction movement. The classification probability for each trial was over 90% that validated the robustness of the trained network to classify three classes of contact states, even with a change of contact direction. This is because the final fingertip deformation in these tests was approximately equal to the trained fingertip condition. Therefore, the trained FNN was able to recognize the contact states even with untrained as well as multiple contact directions.

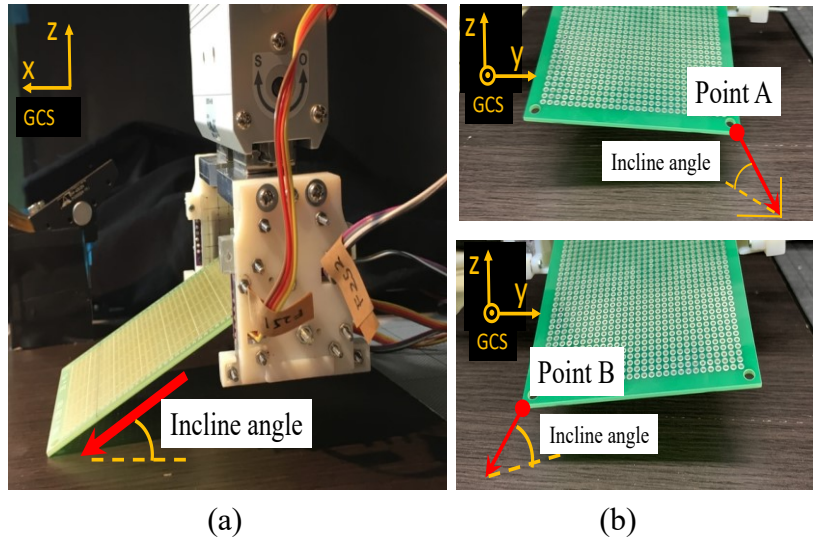


Figure 22. Contact direction movement of the arm for (a) edge contact, and (b) Point A and B contact.

Table 8. Result of untrained contact directions

Classification result			
Point A	Point B	Edge	Average
1.0000	0.9995	0.9751	0.9962

5.2 Electrical inverter

5.2.1 Calibration setup

The setup for estimation of contact state test with electrical frequency inverter (FR-A820, Mitsubishi Electric Co. Ltd., Japan) was performed, as shown in Figure 23. Part A (lid part) of the inverter was put on the sponge. Part B (body part) was attached to the 3-axis sensor, which was fixed on the ground. The arm was moved to grasp Part A, as shown in Figure 24(a). Then, Part A was gripped by the fingertips with the gripping velocity of 5 mm/s and the given grasping displacement of 4 mm. Hall sensors' output and z-axis force data were

measured and taken as the initial value. Next, Part A was picked up and moved to the initial position of the insertion assembly task as given in Figure 24 (b). The arm's flange was rotated along the y-axis of the global coordinate system (GCS) for 10° , and it was recorded as state 0 as shown in Figure 25(a). At this state, the x-axis rotation of flange along GCS was 0° . To prepare the calibration data set, Part A was collided to Part B with three contact states, e.g., states 1–3, as given in Figure 25(b)–(d). State 1 is defined as Part A was perfectly inserted into Part B, State 2 is defined as the left clip of Part A collided with Part B, and State 3 is described as the right clip of Part A was collided with Part B during insertion task. To perform the insertion task, Part A was moved in z-direction GCS from the initial insertion position and contacted Part B with a collision depth of 5 mm. During insertion motion, the MFD values and z-axis force data were recorded. The initial values were subtracted from the data recorded during each contact state to remove offsets. Ten trials were repeated for each contact state condition. For each condition, seven data sets were taken for calibration of the input data, and three data sets were used for the validation test.

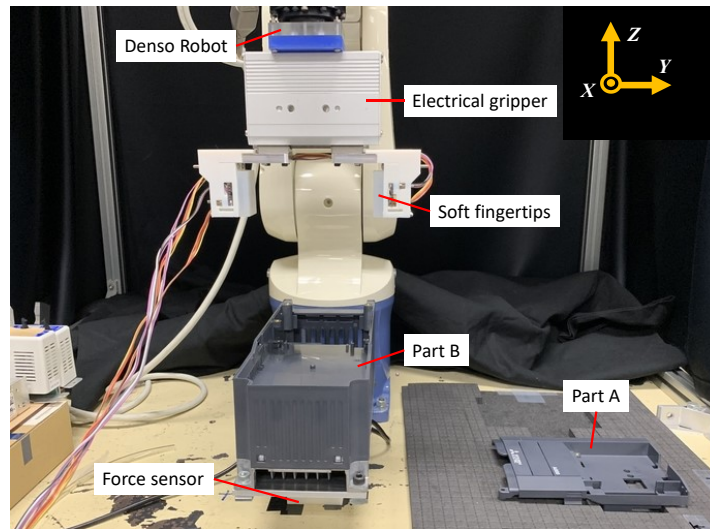
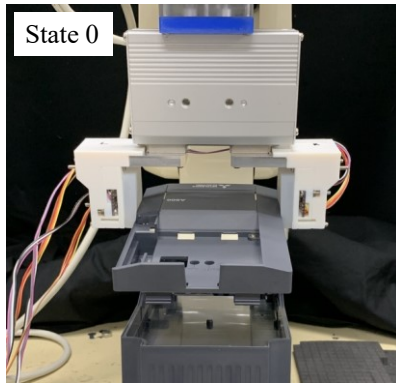


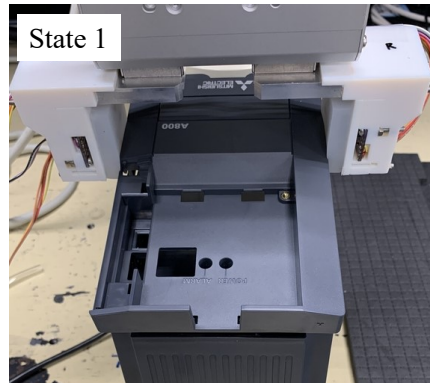
Figure 23. Experimental setup for contact state estimation.



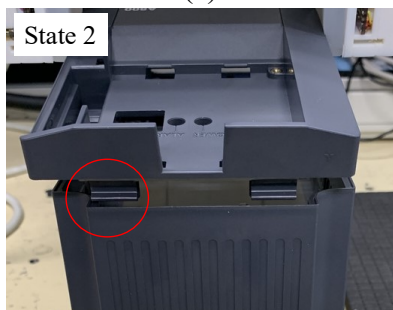
Figure 24. (a) Part A was grasped by the gripper. (b) Part A was picked up to the initial insertion position that was approximately 20 mm above Part B.



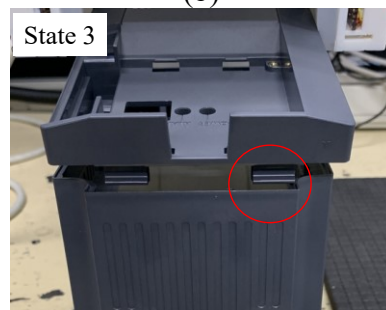
(a)



(b)



(c)



(d)

Figure 25. The contact state definition: (a) state 0, (b) state 1, (c) state 2, and (d) state 3.

Next, the selection of sensor signals ranges for calibrating the network classifier is given. For contact state 1, the normal force, F_z of 0.3 N – 0.5 N was taken as the input of the calibration data set, as shown by the red rectangle in Figure 26(a). The Hall sensor signals with the corresponding normal force were used for the calibration data set of State 1 (Figure 26(b)). Then, for state 2 and 3, the normal force with the range of 0.6 N – 0.8 N was selected, and the Hall sensor signals with the corresponding force were taken as the input for calibration data set of State 2 and 3 accordingly, as shown in Figure 26(c) –(f).

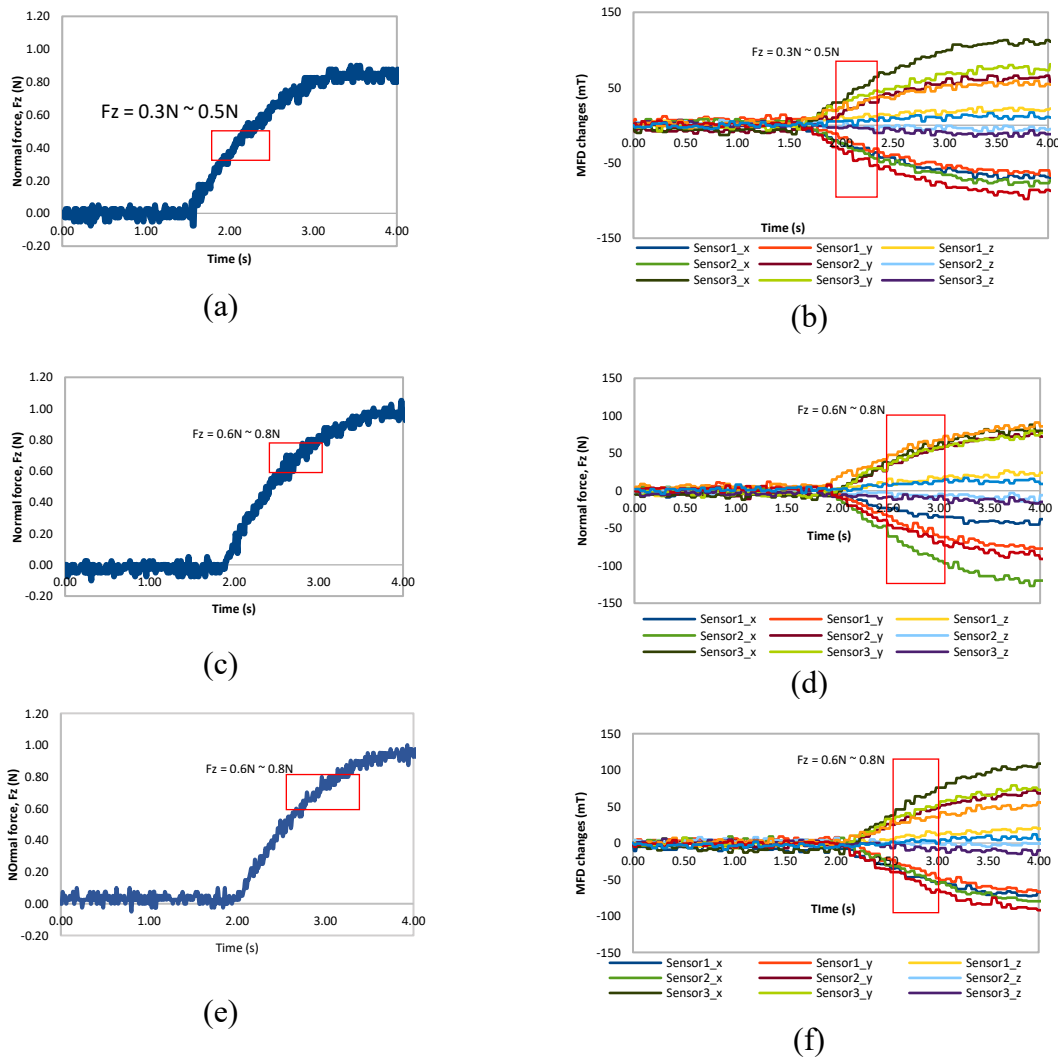
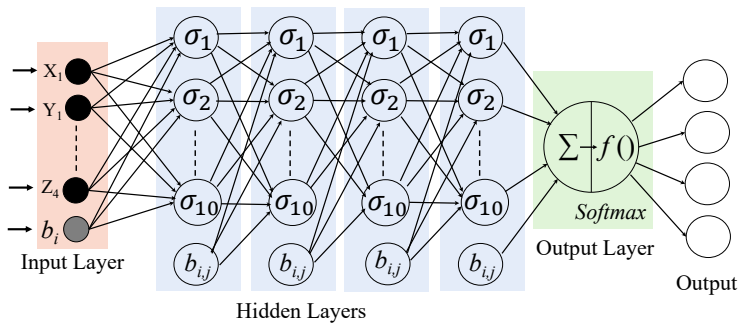
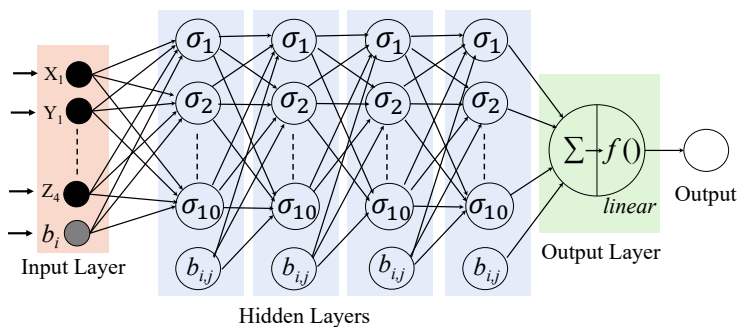


Figure 26. The range of normal force and Hall sensor data to be input into calibration data sets for (a)–(b) State 1, (c)–(d) State 2, and (e)–(f) State 3.

Figure 27 (a)–(b) shows network architectures to estimate contact state between Part A and Part B, and normal contact force, F_z . Two FNNs were constructed using Tensorflow and Keras library, with Python programming language. The networks have 12 input signals, which are MFD changes of Hall sensors. The outputs are the classified of four contact states. In both networks, four hidden layers consisting of ten neurons were applied for calibration. The tan-sigmoid transfer function was used as the activation function to the hidden layer. In the calibration process, the iteration was restricted to 10000 steps. The weights and biases of each layer were calculated to find the relationship between MFD changes, and contact state and normal force.



(a)



(b)

Figure 27. Neural network architecture with four hidden layers to estimate (a) contact state and (b) normal force of electrical inverter.

5.2.2 Assessment tests

Two assessment tests were conducted to validate the performance of the trained network classifier with: (a) untrained flange orientation and (b) untrained grasping position.

(a) Assessment with untrained flange orientation

In the first assessment, Part A was collided with the flange orientation different from the calibration's condition. For contact state 1, the flange was rotated along the y-axis of GCS for 15° from the initial insertion position (Figure 24(b)). Then, Part A was collided with Part B in the z-direction movement for 5 mm collision displacement. Ten validation trials were performed. The estimated contact state, along with the measured and estimated normal force was plotted for each trial as given in Figure 28. We found that FNN can successfully identify the contact state as State 1 for each trial during the insertion task of Part A into Part B. The estimated normal force was behaved similarly, proving that the trained FNN was able to estimate force in a good performance.

For contact states 2 and 3, the flange was rotated along the y-axis of GCS for 15° from the initial insertion position. Then, the flange was rotated along the x-axis of GCS for 5° to a position of untrained flange orientation, as given in Figure 29(a) –(b). Part A was moved vertically to make contact with State 2 and 3 accordingly. Ten trials were repeated for validation data sets. The result for assessment with untrained flange orientation up to measured normal force 0.5 N for contact state 2 is given in Figure 30(a) –(j). The result shows that the trained FNN was able to estimate State 2 during the collision. The fluctuation between estimated State 1 and State 2 occurred in Figure 30(a), (b), (f), and (g). However, in the proposed feedback control system that will be explained in Section 5.3.1, the system will detect State 2 as false insertion assembly once State 2 was detected. Next, the result for

contact state 3 is presented in Figure 31(a)–(j). We found that the FNN was successfully able to estimate State 3 during collision for each trial. Table 9 presents the normal force required for the network classifier to detect the corresponding contact states during the collision. It is noted that the normal force required for estimating State 2 and 3 are approximately 0.32 N and 0.33 N respectively, which are higher compared to State 1 that require 0.16 N. It can be concluded that the fingertip requires a given normal force to deform in order to generate features in sensor signals for estimating the contact states.

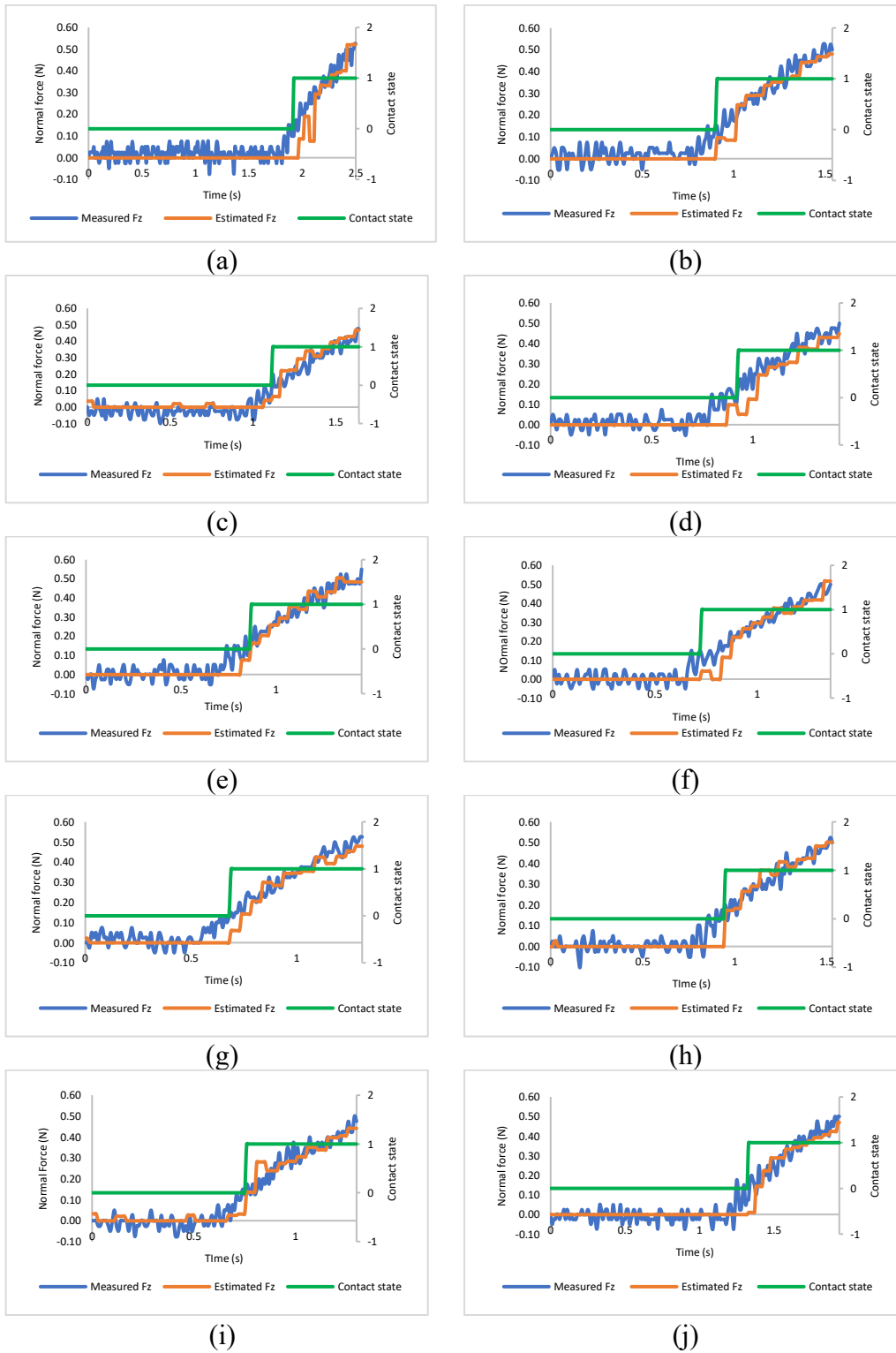


Figure 28. (a)–(j) Ten trials validation test of State 1 with untrained flange orientation, 15°.

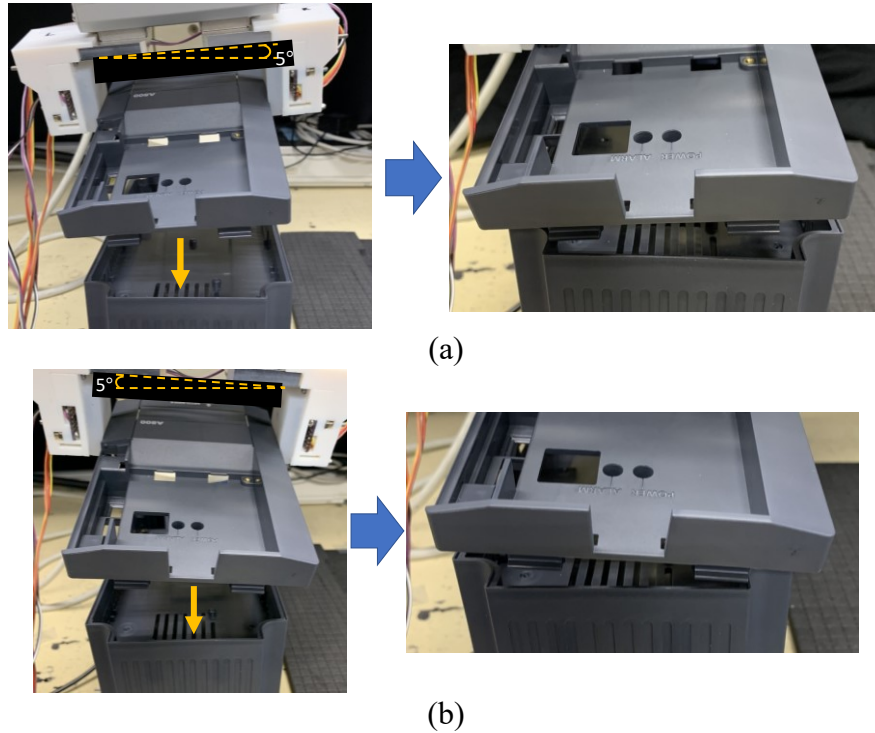


Figure 29. Part A was collided to Part B with untrained flange orientation (rotated 15° along y-axis GCS and 5° along x-axis GCS) for (a) state 2 and (b) state 3.

Table 9. Normal force required for the trained FNN to detect the corresponding contact states.

	Trial 1	Trial 2	Trial 3	Trial 4	Trial 5	Trial 6	Trial 7	Trial 8	Trial 9	Trial 10	Average
Force for State 1 (N)	0.10	0.15	0.20	0.20	0.15	0.13	0.15	0.20	0.18	0.17	0.16
Force for State 2 (N)	0.30	0.17	0.35	0.38	0.42	0.25	0.32	0.35	0.38	0.28	0.32
Force for State 3 (N)	0.23	0.48	0.30	0.25	0.38	0.32	0.35	0.32	0.30	0.38	0.33

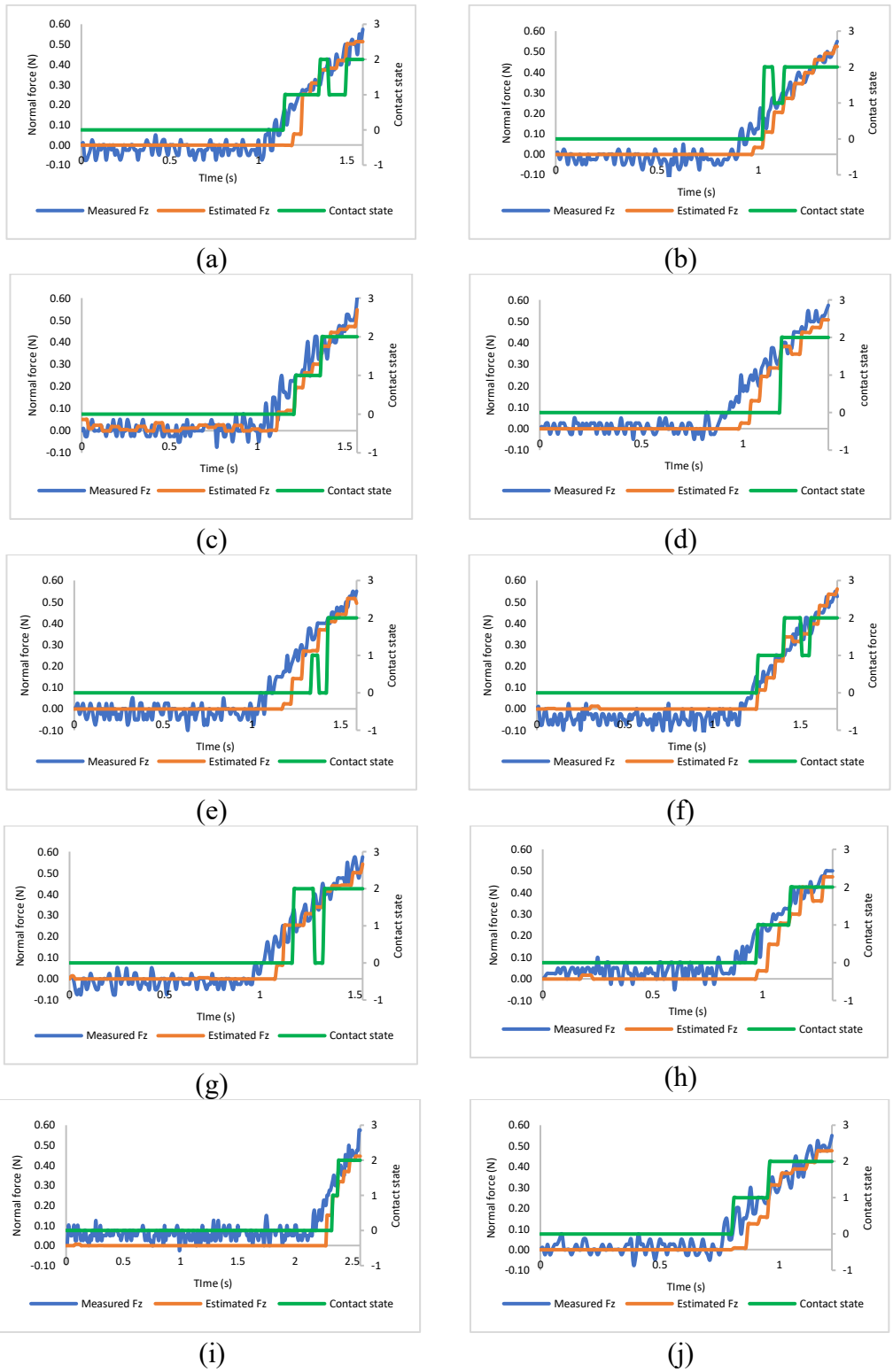


Figure 30. (a)–(j) Ten trials validation test of State 2 with untrained flange orientation.

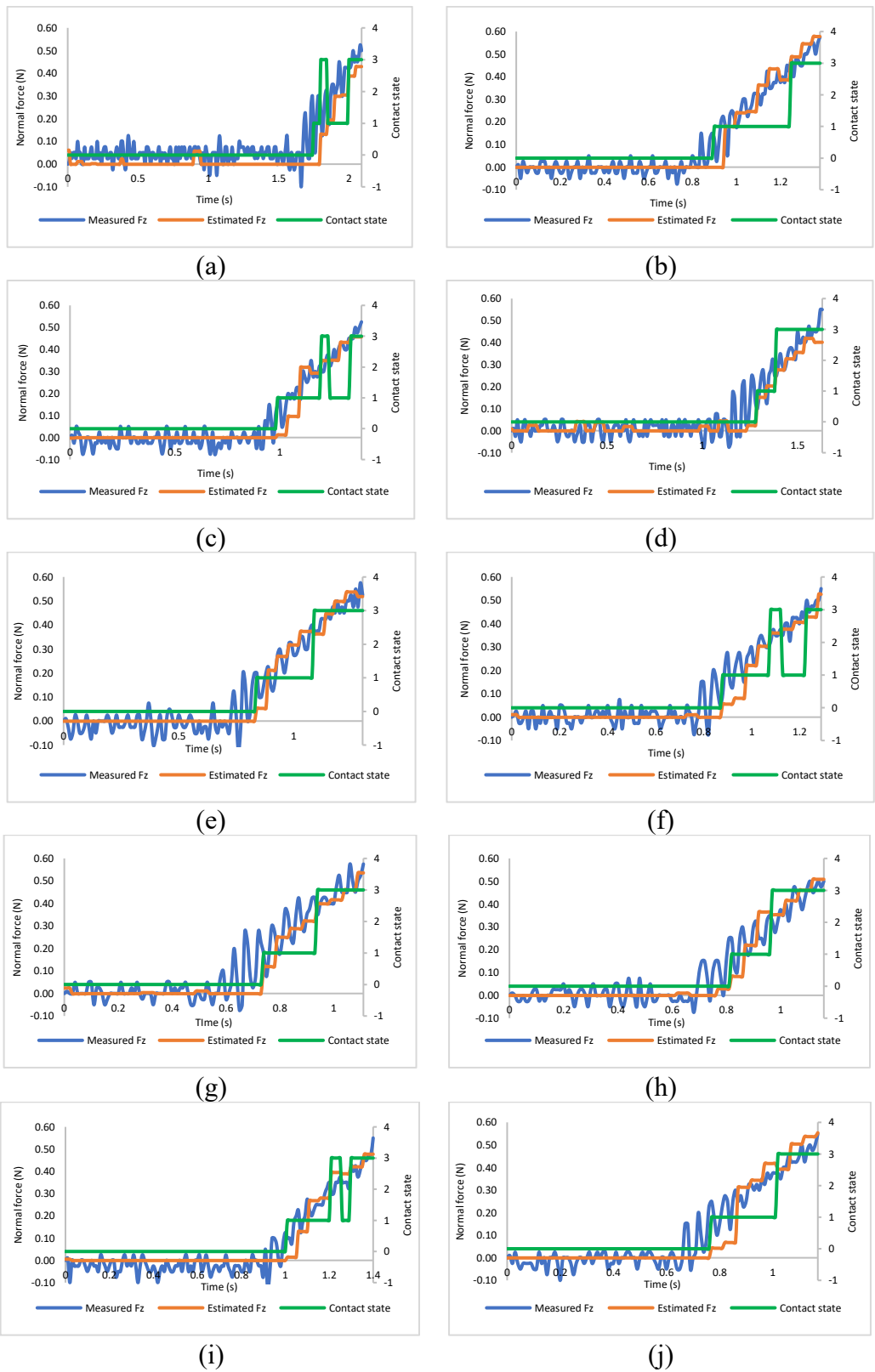


Figure 31. (a)–(j) Ten trials validation test of State 3 with untrained flange orientation.

(b) Assessment with untrained grasping position

In the second assessment, Part A was grasped with different grasping positions from the calibration's condition. The gripper was displaced +5 mm from the origin position of grasping calibration, as illustrated in Figure 32. The same grasping displacement of 4 mm was applied. To conduct the insertion task with different contact states for validation, the arm's flange was rotated along the y-axis of GCS for 10°. The x-axis rotation of GCS was remained 0°. Part A was collided to Part B with different contact states, with five trials for each state. Figure 33–Figure 35 gives the result of the estimated contact state respectively. We found that the proposed fingertip was able to classify the corresponding contact states successfully. Table 10 shows the required normal force to detect the contact states. We found that the required force was below 0.5 N for each trial. The above procedures were repeated for the grasping position with displacement -5 mm from the origin position, and the results are given in Figure 36–Figure 38. It shows that the contact states were successfully able to be determined for each trial. Table 11 provides the required normal force in the condition of -5 mm of displaced grasping position. It can be observed that the required force was within 0.5 N for each trial. Therefore, overall, it can be concluded that the FNN was able to classify the contact states of the inverter even with the condition of untrained grasping position.

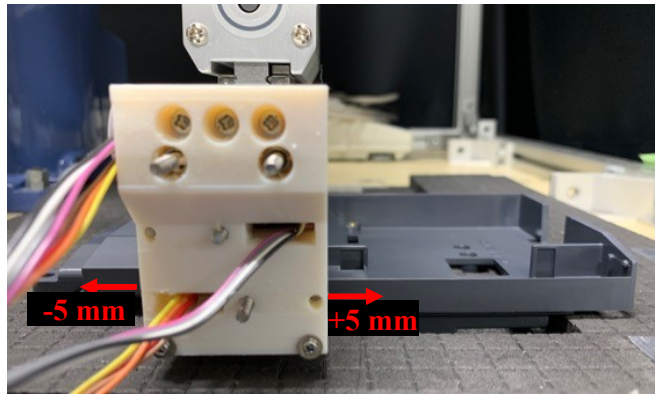


Figure 32. Part A was grasped with untrained grasping position of displaced +5 mm and -5 mm position.

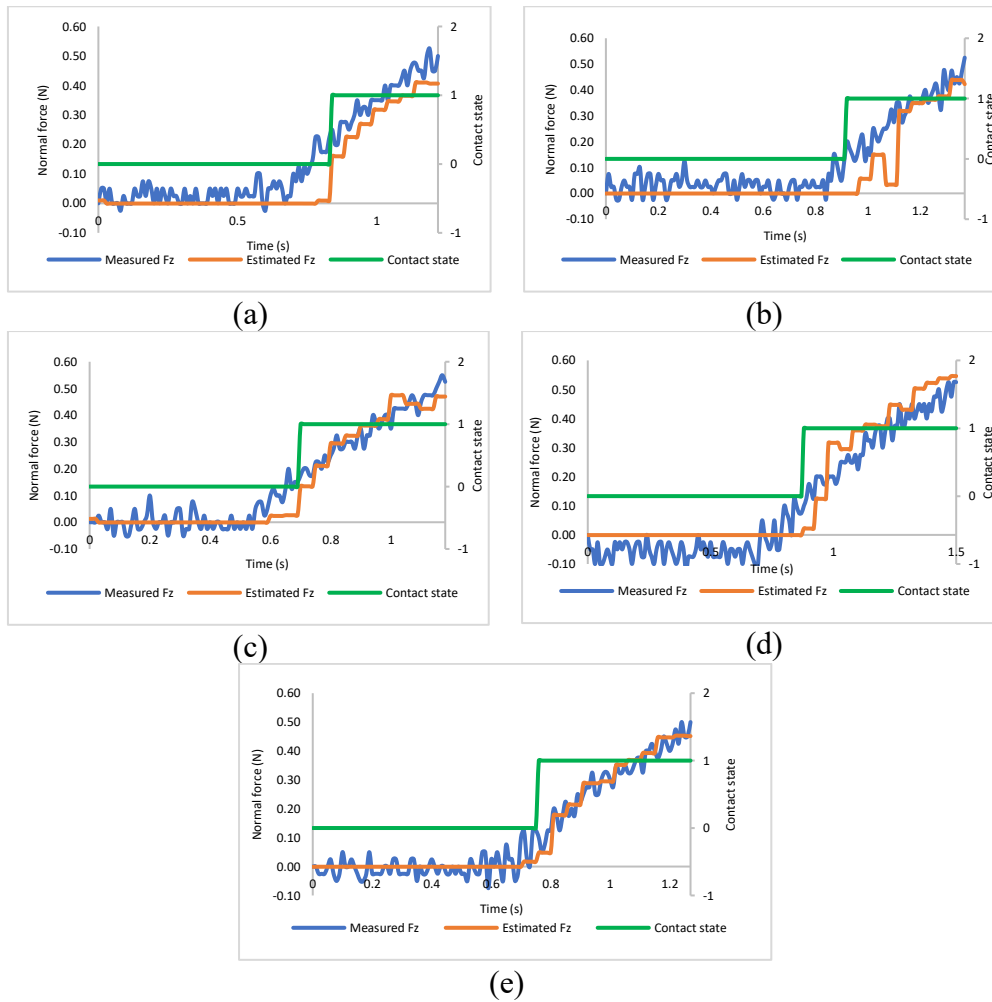


Figure 33. (a)–(e) Five trials validation test of State 1 with untrained grasping position +5 mm.

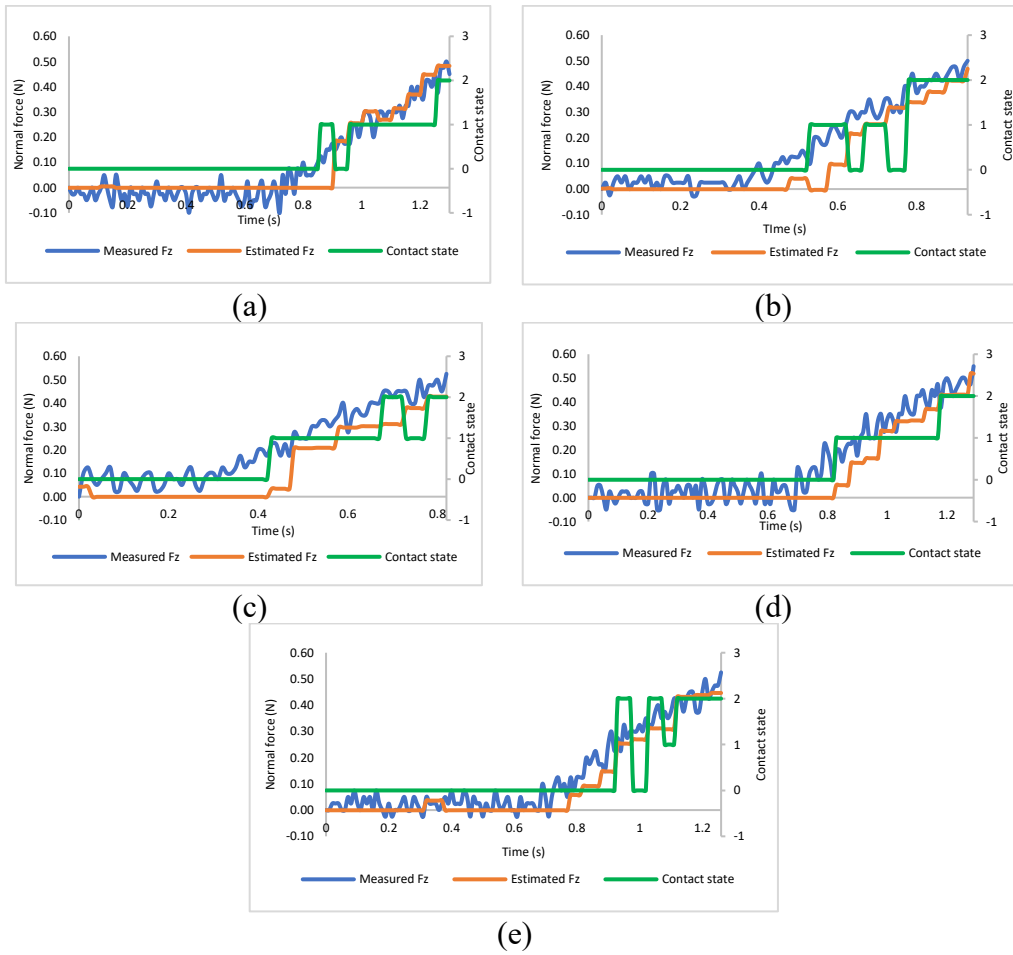


Figure 34. Five trials validation test of State 2 with untrained grasping position +5 mm.

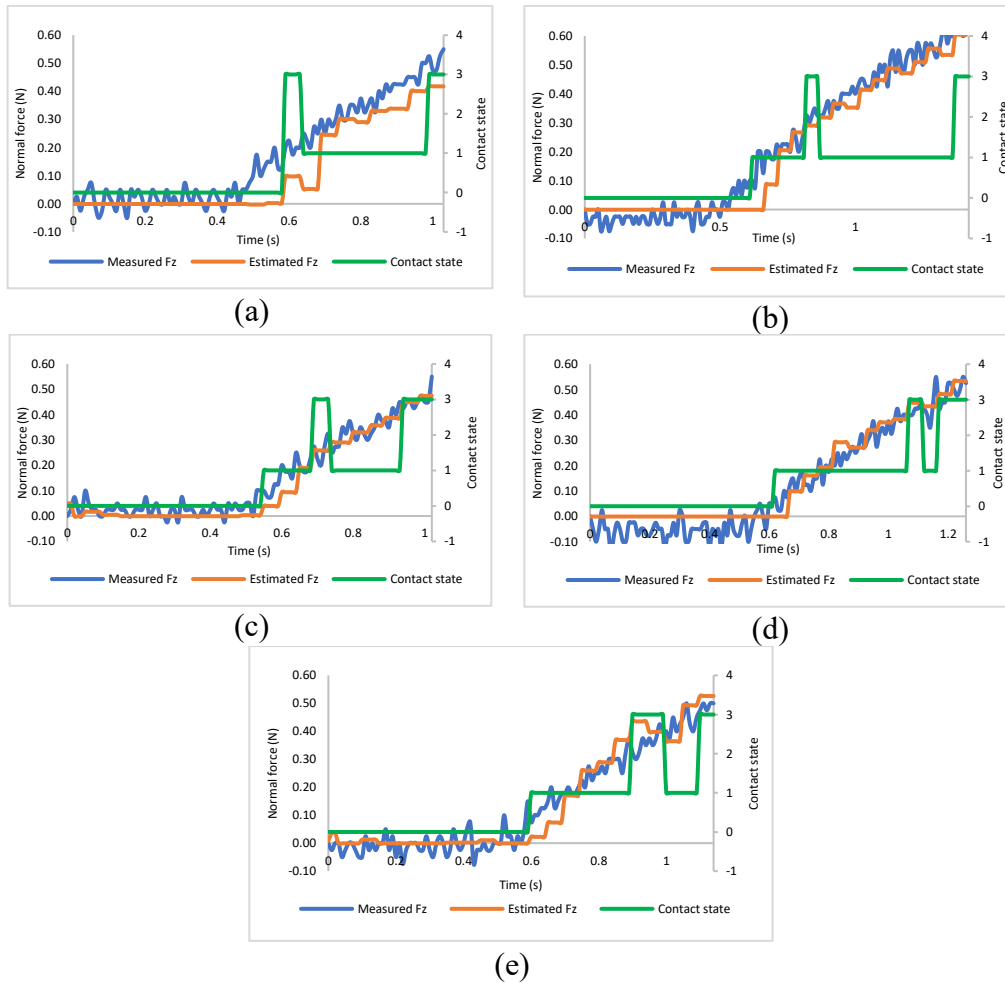


Figure 35. Five trials validation test of State 3 with untrained grasping position +5 mm.

Table 10. Normal force required to detect the corresponding contact states with untrained grasping position of +5 mm.

	Trial 1	Trial 2	Trial 3	Trial 4	Trial 5	Average
Force for State 1 (N)	0.25	0.20	0.17	0.10	0.10	0.16
Force for State 2 (N)	0.38	0.40	0.45	0.38	0.28	0.39
Force for State 3 (N)	0.20	0.32	0.28	0.40	0.32	0.30

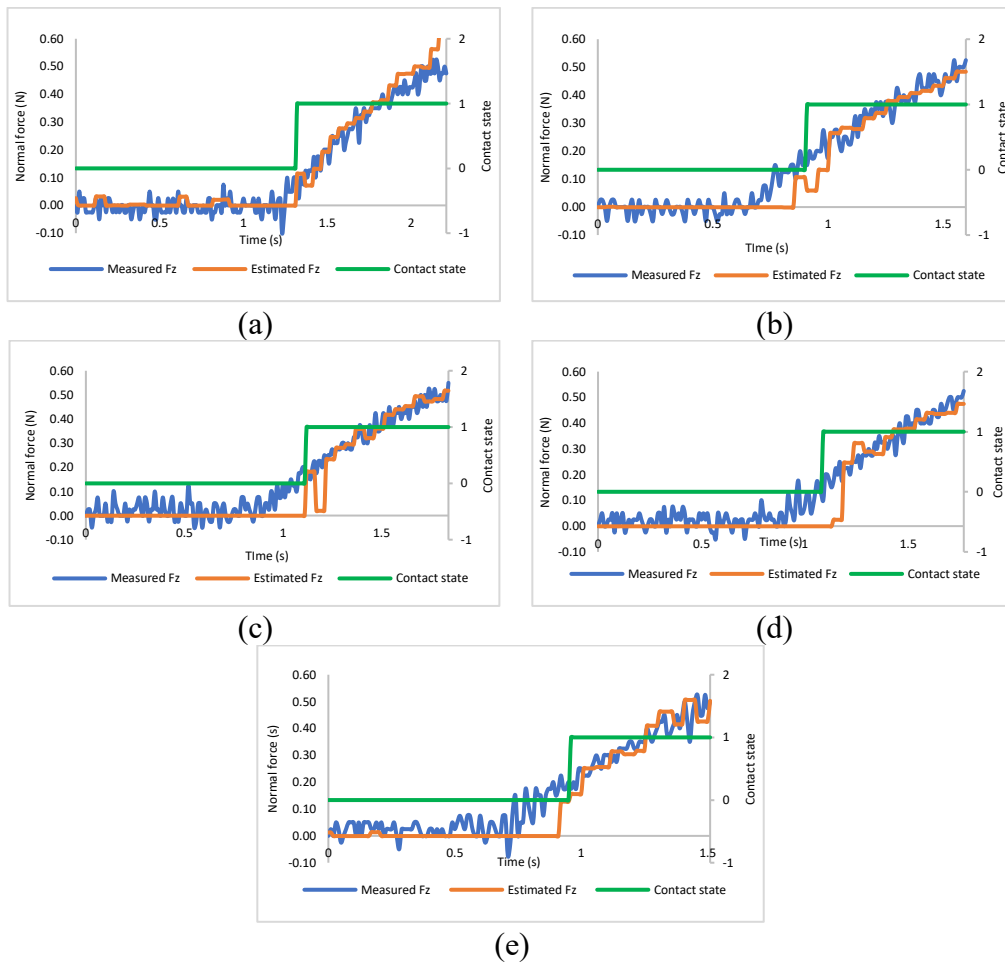


Figure 36. Five trials validation test of State 1 with untrained grasping position -5 mm.

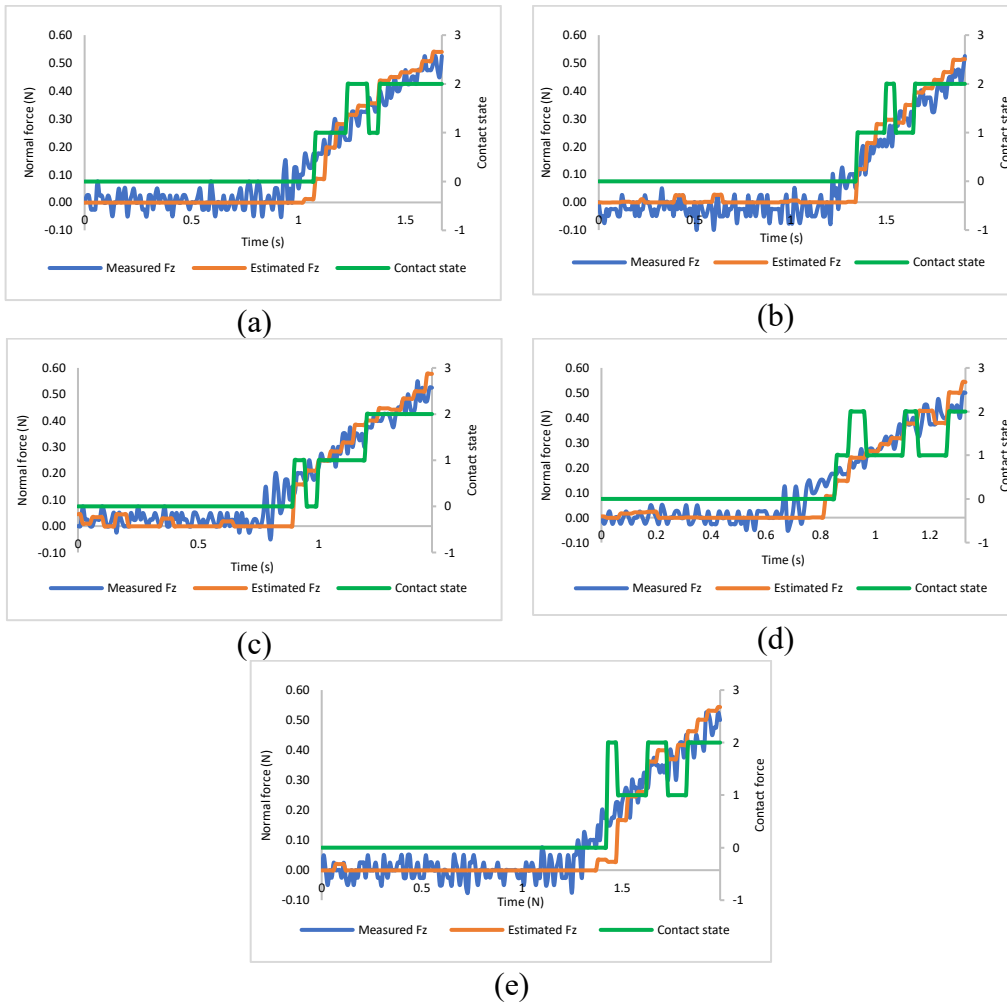


Figure 37. Five trials validation test of State 2 with untrained grasping position -5 mm.

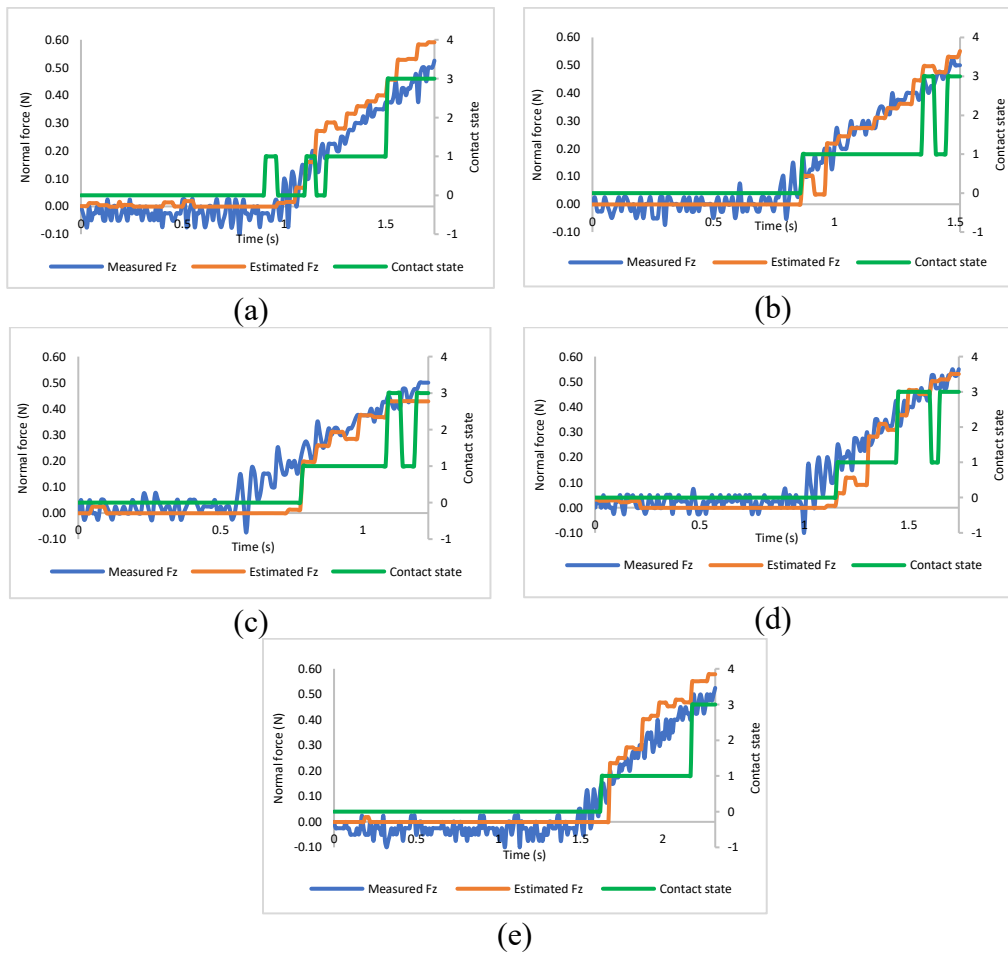


Figure 38. Five trials validation test of State 3 with untrained grasping position -5 mm.

Table 11. Normal force required to detect the corresponding contact states with untrained grasping position of -5 mm.

	Trial 1	Trial 2	Trial 3	Trial 4	Trial 5	Average
Force for State 1 (N)	0.08	0.15	0.15	0.10	0.17	0.13
Force for State 2 (N)	0.23	0.20	0.38	0.23	0.28	0.26
Force for State 3 (N)	0.38	0.45	0.45	0.38	0.45	0.42

5.3 Experimental test of part assembly condition classification and feedback control

In this subchapter, the fingertip was applied to detect false insertion state during assembly task, and then this information was feedbacked to the arm. The arm received the false state signals and move back to the initial insertion position. Denso Robot was employed to perform the feedback control system.

5.3.1 Feedback of false insertion detection

In this study, a false insertion state is defined as State 2 and 3 (Figure 25(c) and (d)), where the clip of Part A collided with Part B. This condition prevents Part A from inserting into Part B to finish the assembly task. This section describes the methodology of the proposed feedback control system of false insertion detection. The program's flow of the control system is given in Figure 39. Initially, the object (Part A) was grasped by the gripper. The measured Hall sensor and normal force data were recorded and taken as the initial value. The arm was moved to the initial position of the insertion assembly (Figure 24(b)). Then, to perform the insertion task, the flange was rotated along y-axis GCS (Figure 25(a)). The measurements were offset by subtracting the initial value. The trained models (in HDF5 format) of contact state classifier and normal force was imported. The contact state and normal force were estimated based on the real-time Hall sensor signals (12 outputs) using Tensorflow and Keras library. The arm was moved to a given target position to perform the insertion assembly task. During insertion, the arm was continuously moved to the given position if the estimated contact state was 0 or 1. However, once the false insertion state, e.g., state 2 or 3, is detected during insertion, the arm is moved back to the initial position of

assembly. This feedback control is introduced to prevent false insertion assembly that may cause damage to the parts. The insertion of the assembly task is finished when the arm reached the given target position.

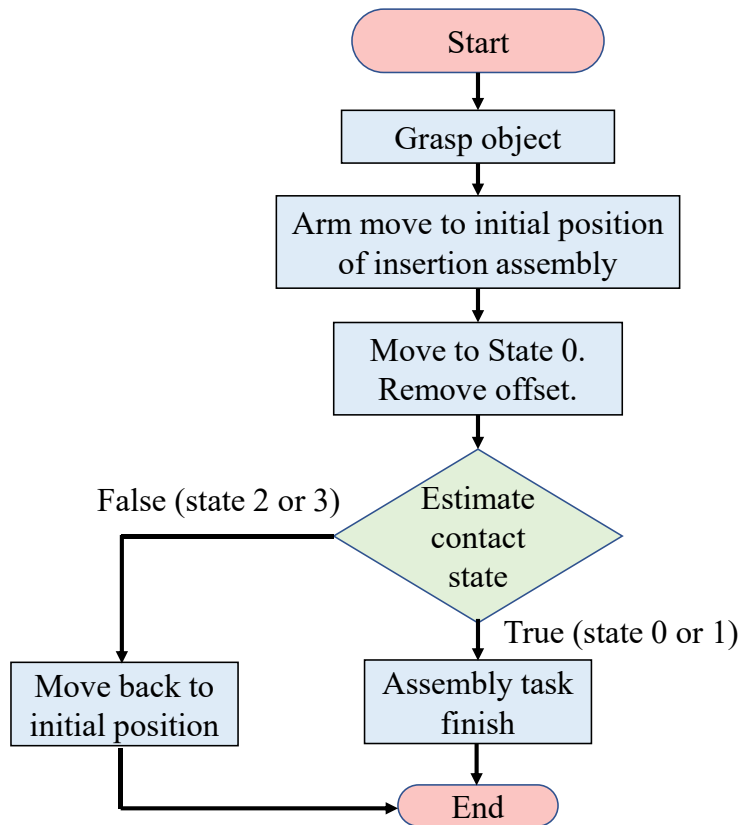


Figure 39. Feedback flowchart.

Figure 40 shows the condition of the perfect insertion of the assembly tasks. Initially, State 0 was estimated. The arm continuously moved to the target position of assembly in z-axis GCS. The network estimated State 1 when reached at the given position, with Part A perfectly inserted into Part B. Meanwhile, Figure 41 presents the scenario of false insertion scenario with left clip collided to Part B, i.e., State 2. The movement of the arm was stopped once State 2 was detected. Then, the arm was moved back upward to the initial position of

assembly. Furthermore, Figure 42 demonstrates the right clip collision, e.g., State 3. It can be observed that the right clip of Part A collided with Part B and State 3 was detected. The arm was stopped and start to move upward towards the initial assembly position.

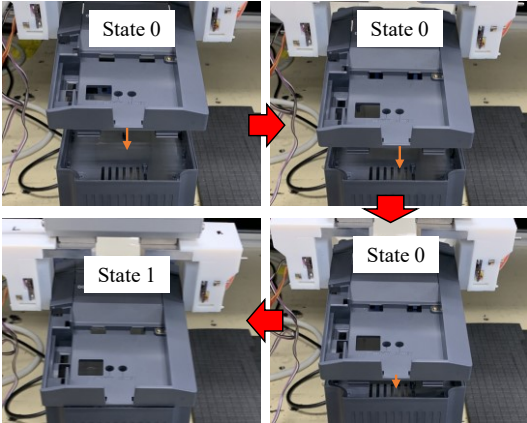


Figure 40. State 1 feedback using Denso Robot.

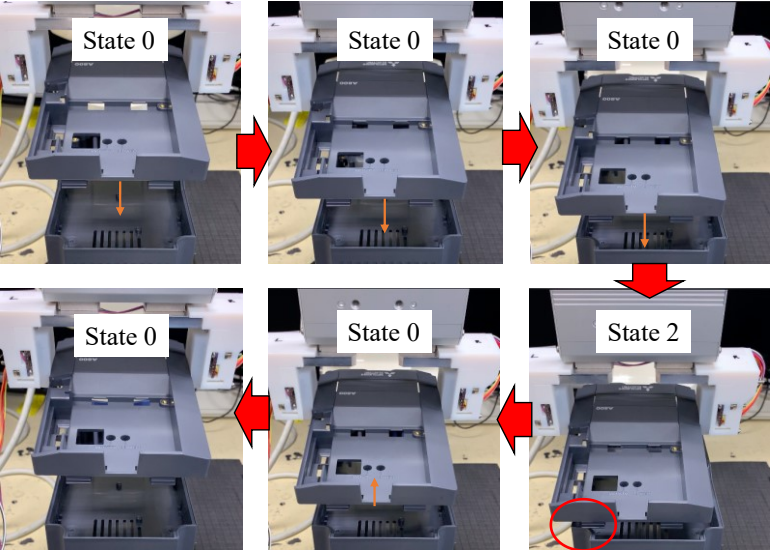


Figure 41. State 2 of feedback using Denso Robot.

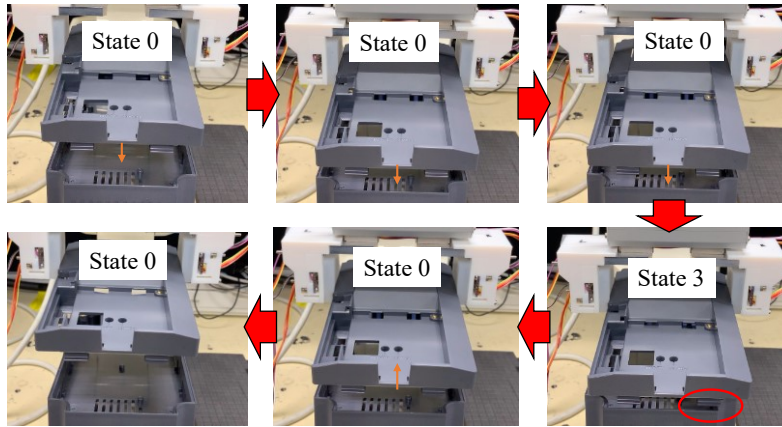


Figure 42. State 3 feedback using Denso Robot

5.3.2 Application with a visual feedback system

The robotic vision has been actively applied in the robotic system for assembly tasks. In [69], the combination of machine vision and tactile sensing to enhance assembly task performance was presented. In addition, by applying deep learning in robotic vision, the stable grasping position could be determined [51]. However, even with the application of robotic vision for assembling parts, the false insertion condition may occur. This could be due to the inaccuracy in grasping parts, template matching algorithms, estimation of target object position, *etc.*

In this section, visual feedback was employed for part insertion task, and the proposed fingertip was employed to detect the false insertion. The experimental setup is presented in Figure 43. The fingertip is attached to a parallel gripper. Part A was put on the sponge. Three cameras (Blasterx Senz3D, Creative Labs, U.S.) were connected to a computer to perform visual feedback, as shown in Figure 44. On Part A, three feature points were placed, represented by red dots in Figure 44. Another three feature points were placed on Part B as the target paired points, represented by blue dots. All six dots' 3D position was estimated using image processing. 6-axis arm (RV-4F, Mitsubishi Electric Co. Ltd, Japan) was applied

to manipulate the inverter. Camera, robotic arm, computer, and Hall sensors were synchronized in the ROS environment. Similarly, a false insertion state is defined as State 2 and 3 as mentioned in Figure 25(c) and (d). In this study, image processing, i.e., a template matching method, was applied to move the arm for grasping tasks. Part A was grasped with a grasping force approximately 5 N. Then, the arm was moved to the initial position of insertion assembly (Figure 44). At this position, the Hall sensor output was measured and taken as the initial value. Then, the real-time measurements were offset by subtracting the initial value. The trained model of contact state classifier was imported into the ROS system, and the contact state was estimated based on Hall sensor signals. To perform the part insertion task, the arm was moved towards Part B to pair both red and blue dots. Figure 45 shows the dots pairing execution, with State 1 condition. When three pairs of dots matched together, State 1 was estimated by the fingertip. The part insertion task was finished, and the robotic motion was stopped.

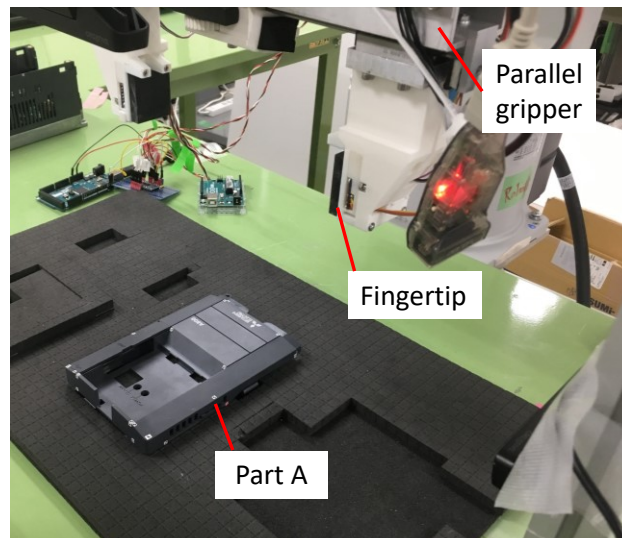


Figure 43. Experimental setup: Part A was put on the sponge. Template matching was applied to grasp the part.

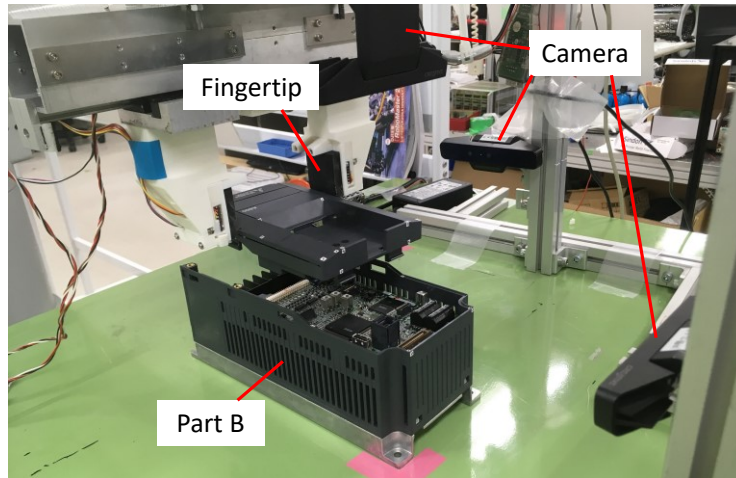


Figure 44. Three cameras were employed to perform visual feedback. The arm was in State 1.

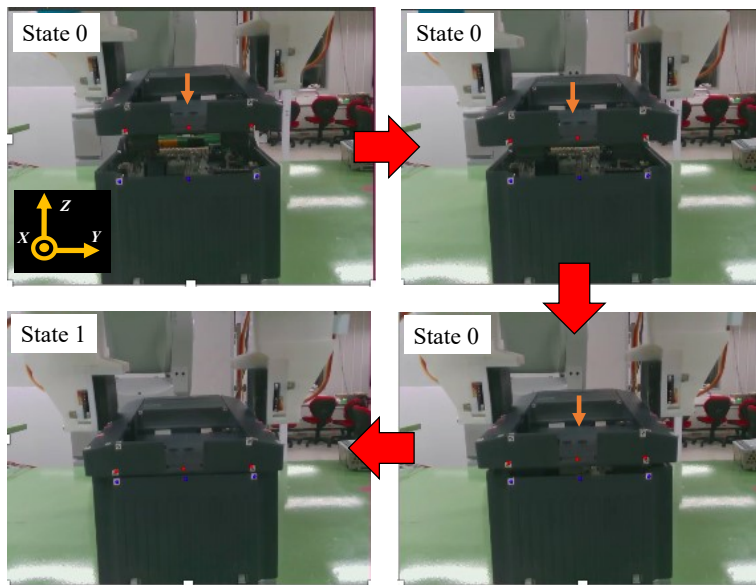


Figure 45. State 1 condition using visual feedback for part insertion.

In Figure 46, the target points (blue dots) were displaced 20 pixels of +y-axis GCS to create false insertion. The left clip Part A was collided with Part A, thus, State 2 was detected. Then, the motion of the arm was stopped, and the arm was moved back upward to initial position of assembly. On the other hand, in Figure 47, the target points were displaced 20

pixels of (-) y-axis GCS to produce false insertion. The right clip of Part A was collided with Part B. Thus, State 3 was detected, and the arm was stopped as the false insertion state has occurred. The arm moved upward towards initial assembly positions.

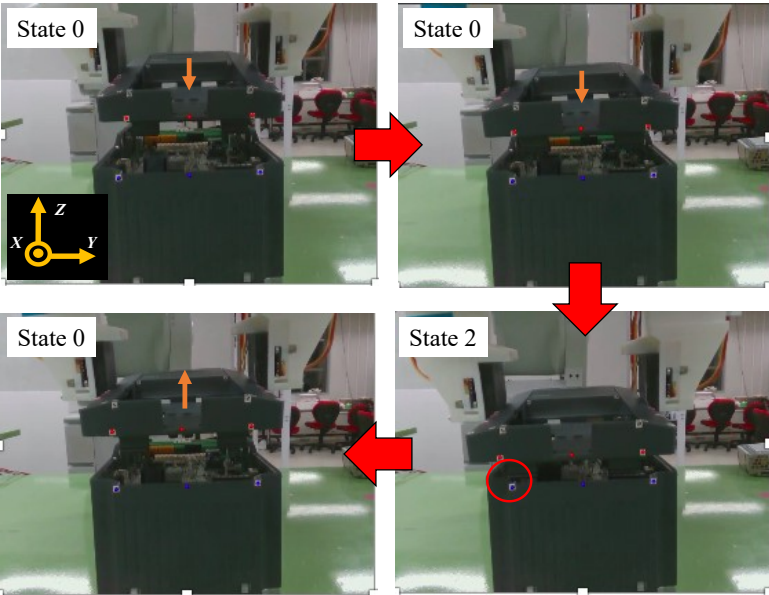


Figure 46. State 2 condition using visual feedback for part insertion.

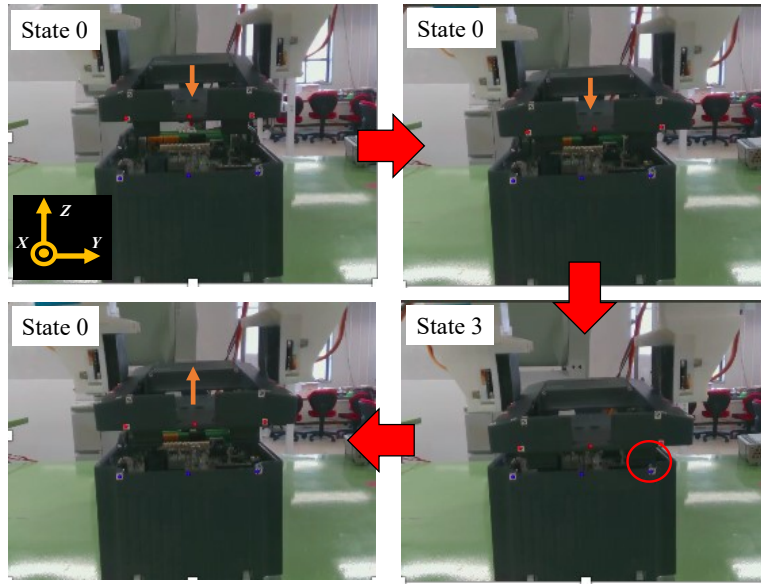


Figure 47. State 3 condition using visual feedback for part insertion.

5.4 Discussion

In this chapter, the contact state classification was performed with a thin rectangular PCB board and an electrical frequency inverter. A rectangular shape of the soft body provides a larger contact area than a hemispherical shape. Larger contact area generates stable and firm grasping. As a result, in Section 5.1, the gripper was able to grasp the thin PCB board and made contact with different states to the planar surface in a firm condition. The contact state was successfully able to be identified even in the condition of both untrained angle of φ and ψ , and untrained contact direction movement. We also repeated the test with the other four contact positions on the fingertip surface. Thus, it is validated that the sensing area of the fingertip was increased compared to our previous design in [44][45]. In Section 5.2, the fingertip was evaluated to discriminate contact states between Part A and Part B of the electrical inverter. We found that the normal force required to estimate State 1–3 is within

0.5 N. It shows that to generate features for classifying contact states during the collision task, the fingertip requires a given force to deform its shape. This normal force value is also representing the sensitivity of the fingertip to classify the target output. To improve the sensor sensitivity, the lower stiffness materials of the soft body can be used. This can allow larger deformation of the fingertip to generate more features in sensor signals. However, it can be noted that slippage could occur due to lower grasping force. Furthermore, by increasing the distribution of embedded magnets along the fingertip surface, the sensitivity of the fingertip could be improved.

The fingertip could be applied to various kinds of objects/parts in industrial assembly applications. In this case, a new calibration is needed to be performed for each part. This is because the MFD changes depend on the contact geometry of objects during grasping; new objects have different edge surfaces, i.e., contact area from the trained objects.

In addition, as we used the measured MFD values from the test as the input into FNN for the training process, the effect of the magnetic interference was assumed to be considered. As a consequence, the crosstalk effect produced by magnetic interference does not significantly affect the fingertip performance.

CHAPTER 6.

Conclusion and Future Works

6.1 Conclusions

Tactile sensors have been playing an essential role in many soft robotics applications, such as in assembly part manipulation, material classification application, surgical application, and dexterous robotic hands. Many designs of magnetic-based tactile sensors have been developed for various objectives, i.e., texture discrimination, force and vibration estimation, object exploration, *etc.* The developed sensors have their advantages and disadvantages. However, there are still unsolved issues that need to be investigated for the improvement of such tactile sensors, i.e., designing Hall effect-based tactile fingertips with a minimal number of sensors and applying such fingertips to estimate the object orientation and contact states for assembly task.

The work presented in this dissertation is mainly focusing on fabrication, modeling and experimental test of the proposed tactile fingertip. It includes the FE model of the soft fingertip to evaluate the sensor performance for contact states classification, fabrication step of a fingertip using a 3D printer and silicone rubber, and experimental validation tests, i.e., object orientation, gripping force estimation and contact states classification. The main contribution of our current work includes:

1. A design of Hall effect-based tactile fingertip was proposed to estimate object orientation, gripping force, and contact state. Through the use of two Hall-effect

sensors, the current design is able to increase the sensing area compared to the past fingertip design in [44], which is limited to only the center of the fingertip surface. We have conducted the experimental tests of object orientation estimation and contact state classification for several contact positions on the fingertip surface and found that the fingertip was successfully able to estimate the target output.

2. A 3D FE model of deformation and magnetic flux density was developed to simulate the proposed sensor outputs. As discussed in Section 1.2, the FE simulation of Hall effect-based soft tactile sensors has not been investigated. The combination of fingertip deformation and magnetic flux density simulation to simulate Hall sensor outputs makes it difficult to simulate the subject accurately. In this study, an FE model of fingertip was constructed to simulate the deformation of the soft body under external force. Then, an FE model of magnetic flux density was created. Based on the simulated MFD distribution, the sensor performance was evaluated to classify different contact states. We found that the fingertip design has generated enough features to classify contact states.
3. A calibration method was presented to estimate the object orientation and gripping force of thin rectangular objects based on MFD changes during grasping motion. A feedforward neural network of six inputs and one hidden layer was constructed to estimate the target outputs. Results show that the network was able to estimate object orientation and gripping force even with untrained contact position and untrained object orientation. Furthermore, we found that the estimation error was increased with the increase in board thickness. Thus, to address this limitation, we made assumption

that, to estimate object orientation in good performance, the grasped object should be within 10% of the minimum width of the sensor surface.

4. A classification method to discriminate contact states during the collision of the grasped objects to the environment was proposed. Based on MFD changes of Hall sensor outputs (12 signals), an FNN was constructed. In the validation test, we presented the classification of contact states for a thin circuit board during the collision with the plane surface. Three contact states were successfully estimated, even with untrained contact positions, untrained object orientation, and untrained contact direction movement. Then, the validation test was conducted with electrical gripper, and the result found that the network was successfully classified the contact states even with the condition of untrained flange orientation and untrained grasping position.
5. A state detection of false insertion during part insertion was presented. It is one alternative solution to prevent further damage to the parts when the false insertion accidentally occurred during part assembly. In this study, the feedback system was constructed in the ROS environment. The arm moved to a target position, and the estimated state was feedback to the arm. If the arm receives false state signals, i.e., states 2 and 3, the arm will move back to the initial insertion position. The test with a 6-axis arm demonstrated that the false state insertion (left and right clip collision) was successfully detected, and the arm moved back upward to the initial insertion position.

6.2 Future works

In the future, the geometrical optimization of the current fingertip design will be investigated. The possible design variables are multiple magnets' position and orientation, soft body dimensions, *etc.* To improve the performance of the fingertip, the maximization of magnet displacement will be set as the objective function. Furthermore, other types of materials, i.e., silicone rubbers, will be considered for fingertip fabrication. Moreover, other machine learning methods will be considered as alternatives. For instance, a deep learning approach will be tested and compared to improve the estimation performance. The crosstalk effect produced by magnetic interference will be further analyzed.

References

- [1] D. Trivedi, C. D. Rahn, W. M. Kier, and I. D. Walker, “Soft robotics: Biological inspiration, state of the art, and future research,” *Appl. Bionics Biomech.*, 2008.
- [2] F. Iida and C. Laschi, “Soft robotics: Challenges and perspectives,” in *Procedia Computer Science*, 2011.
- [3] Z. Wang, M. Z. Q. Chen, and J. Yi, “Soft robotics for engineers,” *HKIE Trans. Hong Kong Inst. Eng.*, 2015.
- [4] C. M. Best, M. T. Gillespie, P. Hyatt, L. Rupert, V. Sherrod, and M. D. Killpack, “A New Soft Robot Control Method: Using Model Predictive Control for a Pneumatically Actuated Humanoid,” *IEEE Robot. Autom. Mag.*, 2016.
- [5] J. Zhou, X. Chen, U. Chang, J. Pan, W. Wang, and Z. Wang, “Intuitive Control of Humanoid Soft-Robotic Hand BCL-13,” in *IEEE-RAS International Conference on Humanoid Robots*, 2019.
- [6] A. Alspach, J. Kim, and K. Yamane, “Design of a soft upper body robot for physical human-robot interaction,” in *IEEE-RAS International Conference on Humanoid Robots*, 2015.
- [7] R. F. Shepherd *et al.*, “Multigait soft robot,” *Proc. Natl. Acad. Sci. U. S. A.*, 2011.
- [8] Y. L. Park *et al.*, “Design and control of a bio-inspired soft wearable robotic device for ankle-foot rehabilitation,” *Bioinspiration and Biomimetics*, 2014.
- [9] A. DeMario and J. Zhao, “A miniature, 3D-printed, walking robot with soft joints,” in *Proceedings of the ASME Design Engineering Technical Conference*, 2017.

- [10] Z. Wang, Y. Torigoe, and S. Hirai, “A Prestressed Soft Gripper: Design, Modeling, Fabrication, and Tests for Food Handling,” *IEEE Robot. Autom. Lett.*, vol. 2, no. 4, pp. 1909–1916, 2017.
- [11] K. C. Galloway *et al.*, “Soft Robotic Grippers for Biological Sampling on Deep Reefs,” *Soft Robot.*, vol. 3, no. 1, pp. 23–33, 2016.
- [12] H. Zhang, A. S. Kumar, F. Chen, J. Y. H. Fuh, and M. Y. Wang, “Topology optimized multimaterial soft fingers for applications on grippers, rehabilitation, and artificial hands,” *IEEE/ASME Trans. Mechatronics*, 2019.
- [13] V. Ho and S. Hirai, “Design and Analysis of a Soft-Fingered Hand With Contact Feedback,” *IEEE Robot. Autom. Lett.*, vol. 2, no. 2, pp. 491–498, 2017.
- [14] J. Morrow *et al.*, “Improving Soft Pneumatic Actuator fingers through integration of soft sensors, position and force control, and rigid fingernails,” in *Proceedings - IEEE International Conference on Robotics and Automation*, 2016.
- [15] R. Adam Bilodeau, E. L. White, and R. K. Kramer, “Monolithic fabrication of sensors and actuators in a soft robotic gripper,” in *IEEE International Conference on Intelligent Robots and Systems*, 2015.
- [16] M. C. Yuen, R. Kramer-Bottiglio, and J. Paik, “Strain sensor-embedded soft pneumatic actuators for extension and bending feedback,” in *2018 IEEE International Conference on Soft Robotics, RoboSoft 2018*, 2018.
- [17] G. Chatzipirpiridis, P. Erne, O. Ergeneman, S. Pane, and B. J. Nelson, “A magnetic force sensor on a catheter tip for minimally invasive surgery,” in *Proceedings of the Annual International Conference of the IEEE Engineering in Medicine and Biology Society, EMBS*, 2015.

- [18] J. Back, P. Dasgupta, L. Seneviratne, K. Althoefer, and H. Liu, “Feasibility study—novel optical soft tactile array sensing for minimally invasive surgery,” in *IEEE International Conference on Intelligent Robots and Systems*, 2015.
- [19] F. L. Hammond, R. K. Kramer, Q. Wan, R. D. Howe, and R. J. Wood, “Soft tactile sensor arrays for force feedback in micromanipulation,” *IEEE Sens. J.*, vol. 14, no. 5, pp. 1443–1452, 2014.
- [20] L. Zhang, F. Ju, Y. Cao, Y. Wang, and B. Chen, “A tactile sensor for measuring hardness of soft tissue with applications to minimally invasive surgery,” *Sensors Actuators, A Phys.*, 2017.
- [21] L. Jamone, L. Natale, G. Metta, and G. Sandini, “Highly sensitive soft tactile sensors for an anthropomorphic robotic hand,” *IEEE Sens. J.*, 2015.
- [22] M. Costanzo, G. De Maria, C. Natale, and S. Pirozzi, “Design and calibration of a force/tactile sensor for dexterous manipulation,” *Sensors (Switzerland)*, 2019.
- [23] S. Pirozzi and C. Natale, “Tactile-Based Manipulation of Wires for Switchgear Assembly,” *IEEE/ASME Trans. Mechatronics*, 2018.
- [24] S. Decherchi, P. Gastaldo, R. S. Dahiya, M. Valle, and R. Zunino, “Tactile-data classification of contact materials using computational intelligence,” *IEEE Trans. Robot.*, vol. 27, no. 3, pp. 635–639, 2011.
- [25] S. S. Baishya and B. Bäuml, “Robust material classification with a tactile skin using deep learning,” in *IEEE International Conference on Intelligent Robots and Systems*, 2016.
- [26] N. Jamali and C. Sammut, “Material classification by tactile sensing using surface textures,” in *Proceedings - IEEE International Conference on Robotics and*

Automation, 2010.

- [27] D. S. Chaturanga, Z. Wang, Y. Noh, T. Nanayakkara, and S. Hirai, “Magnetic and Mechanical Modeling of a Soft Three-Axis Force Sensor,” *IEEE Sens. J.*, vol. 16, no. 13, pp. 5298–5307, 2016.
- [28] D. S. Chaturanga, Z. Wang, Y. Noh, T. Nanayakkara, and S. Hirai, “A soft three axis force sensor useful for robot grippers,” in *IEEE International Conference on Intelligent Robots and Systems (IROS)*, 2016, pp. 5556–5563.
- [29] A. Dwivedi, A. Ramakrishnan, A. Reddy, K. Patel, S. Ozel, and C. D. Onal, “Design, Modeling, and Validation of a Soft Magnetic 3-D Force Sensor,” *IEEE Sens. J.*, vol. 18, no. 9, pp. 3852–3863, 2018.
- [30] T. Kawasetsu, T. Horii, H. Ishihara, and M. Asada, “Mexican-hat-like response in a flexible tactile sensor using a magnetorheological elastomer,” *Sensors*, vol. 18, no. 2, 2018.
- [31] T. Kawasetsu, T. Horii, H. Ishihara, and M. Asada, “Deformation response of a magnetic type tactile sensor with a two-layered surface made of a non-magnetic and a magnetorheological elastomer,” *J. Japan Soc. Appl. Electromagn. Mech.*, vol. 24, no. 3, pp. 204–209, 2016.
- [32] D. S. Chaturanga, Z. Wang, Y. Noh, T. Nanayakkara, and S. Hirai, “Robust real time material classification algorithm using soft three axis tactile sensor: Evaluation of the algorithm,” in *IEEE International Conference on Intelligent Robots and Systems*, 2015.
- [33] M. Goka, H. Nakamoto, and S. Takenawa, “A magnetic type tactile sensor by GMR elements and inductors,” in *IEEE/RSJ 2010 International Conference on Intelligent Robots and Systems, IROS 2010 - Conference Proceedings*, 2010.

- [34] Y. Liu, H. Han, T. Liu, J. Yi, Q. Li, and Y. Inoue, “A novel tactile sensor with electromagnetic induction and its application on stick-slip interaction detection,” *Sensors (Switzerland)*, 2016.
- [35] L. Jamone, G. Metta, F. Nori, and G. Sandini, “James: A humanoid robot acting over an unstructured world,” in *Proceedings of the 2006 6th IEEE-RAS International Conference on Humanoid Robots, HUMANOIDS*, 2006.
- [36] T. Paulino *et al.*, “Low-cost 3-axis soft tactile sensors for the human-friendly robot Vizzy,” in *Proceedings - IEEE International Conference on Robotics and Automation*, 2017, pp. 966–971.
- [37] H. Mirzanejad and M. Agheli, “Soft force sensor made of magnetic powder blended with silicone rubber,” *Sensors Actuators, A Phys.*, 2019.
- [38] T. P. Tomo *et al.*, “A New Silicone Structure for uSkin - A Soft, Distributed, Digital 3-Axis Skin Sensor and Its Integration on the Humanoid Robot iCub,” *IEEE Robot. Autom. Lett.*, vol. 3, no. 3, pp. 2584–2591, 2018.
- [39] T. P. Tomo *et al.*, “Covering a Robot Fingertip with uSkin: A Soft Electronic Skin with Distributed 3-Axis Force Sensitive Elements for Robot Hands,” *IEEE Robot. Autom. Lett.*, vol. 3, no. 1, pp. 124–131, 2018.
- [40] K. T. Andrzejewski, M. P. Cooper, C. A. Griffiths, and C. Giannetti, “Optimisation process for robotic assembly of electronic components,” *Int. J. Adv. Manuf. Technol.*, 2018.
- [41] S. Youssefian, N. Rahbar, and E. Torres-Jara, “Contact behavior of soft spherical tactile sensors,” *IEEE Sens. J.*, vol. 14, no. 5, pp. 1435–1442, 2014.
- [42] H. Wang *et al.*, “A Low-cost Soft Tactile Sensing Array Using 3D Hall Sensors,” in

Procedia Engineering, 2016, pp. 650–653.

- [43] Z. Kappassov, D. Baimukashev, O. Adiyatov, S. Salakchinov, Y. Massalin, and H. A. Varol, “A Series Elastic Tactile Sensing Array for Tactile Exploration of Deformable and Rigid Objects,” in *IEEE International Conference on Intelligent Robots and Systems*, 2018, pp. 520–525.
- [44] M. H. B. Rosle, R. Kojima, Z. Wang, and S. Hirai, “Soft Fingertip with Tactile Sensation for Detecting Grasping Orientation of Thin Object,” in *2018 IEEE International Conference on Robotics and Biomimetics, ROBIO 2018*, 2018, pp. 1304–1309.
- [45] M. H. Rosle, Z. Wang, and S. Hirai, “Geometry Optimisation of a Hall-Effect-Based Soft Fingertip for Estimating Orientation of Thin Rectangular Objects,” *Sensors (Basel)*, vol. 19, no. 18, p. 4056, 2019.
- [46] M. H. Rosle, R. Kojima, K. Or, Z. Wang, and S. Hirai, “Soft Tactile Fingertip to Estimate Orientation and the Contact State of Thin Rectangular Objects,” *IEEE Robot. Autom. Lett.*, vol. 5, no. 1, pp. 159–166, 2020.
- [47] B. Winstone, G. Griffiths, C. Melhuish, T. Pipe, and J. Rossiter, “TACTIP - Tactile fingertip device, challenges in reduction of size to ready for robot hand integration,” in *2012 IEEE International Conference on Robotics and Biomimetics, ROBIO 2012 - Conference Digest*, 2012, pp. 160–166.
- [48] K. Shimonomura and H. Nakashima, “A combined tactile and proximity sensing employing a compound-eye camera,” in *Proceedings of IEEE Sensors*, 2013.
- [49] S. Dong, W. Yuan, and E. H. Adelson, “Improved GelSight tactile sensor for measuring geometry and slip,” in *IEEE International Conference on Intelligent Robots*

and Systems, 2017.

- [50] M. K. Kang, S. Lee, and J. H. Kim, “Shape optimization of a mechanically decoupled six-axis force/torque sensor,” *Sensors Actuators, A Phys.*, vol. 209, pp. 41–51, 2014.
- [51] I. Lenz, H. Lee, and A. Saxena, “Deep learning for detecting robotic grasps,” *Int. J. Rob. Res.*, vol. 34, no. 4, pp. 705–724, 2015.
- [52] A. D’Amore, G. De Maria, L. Grassia, C. Natale, and S. Pirozzi, “Silicone-rubber-based tactile sensors for the measurement of normal and tangential components of the contact force,” *J. Appl. Polym. Sci.*, 2011.
- [53] N. Xydas, M. Bhagavat, and I. Kao, “Study of soft-finger contact mechanics using finite elements analysis and experiments,” in *Proceedings - IEEE International Conference on Robotics and Automation*, 2000.
- [54] V. A. Ho and S. Hirai, “A novel model for assessing sliding mechanics and tactile sensation of human-like fingertips during slip action,” *Rob. Auton. Syst.*, vol. 63, pp. 253–267, 2015.
- [55] A. V. Ho and S. Hirai, “Three-dimensional beam bundle model of a sliding soft fingertip,” in *Springer Tracts in Advanced Robotics*, 2014.
- [56] Z. Wang, L. Wang, V. A. Ho, S. Morikawa, and S. Hirai, “A 3-D nonhomogeneous FE model of human fingertip based on MRI measurements,” *IEEE Trans. Instrum. Meas.*, vol. 61, no. 12, pp. 3147–3157, 2012.
- [57] F. Barbagli, A. Frisoli, K. Salisbury, and M. Bergamasco, “Simulating human fingers: A soft finger proxy model and algorithm,” in *Proceedings - 12th International Symposium on Haptic Interfaces for Virtual Environment and Teleoperator Systems, HAPTICS*, 2004, pp. 9–17.

- [58] M. Pozzi *et al.*, “Efficient FEM-Based simulation of soft robots modeled as kinematic chains,” in *Proceedings - IEEE International Conference on Robotics and Automation*, 2018.
- [59] I. F. Jasim and P. W. Plapper, “Contact-state monitoring of force-guided robotic assembly tasks using expectation maximization-based Gaussian mixtures models,” *Int. J. Adv. Manuf. Technol.*, vol. 73, no. 5–8, pp. 623–633, 2014.
- [60] M. W. Abdullah, H. Roth, M. Weyrich, J. Wahrburg, and P. Pluemworasawat, “Force/Torque data modeling for contact position estimation in peg-in-hole assembling application,” in *MATEC Web of Conferences*, 2015.
- [61] D. Ortega-Aranda, I. Lopez-Juarez, B. Nath-Saha, R. Osorio-Comparan, M. Peña-Cabrera, and G. Lefranc, “Towards learning contact states during peg-in-hole assembly with a dual-arm robot,” in *2017 CHILEAN Conference on Electrical, Electronics Engineering, Information and Communication Technologies, CHILECON 2017 - Proceedings*, 2017.
- [62] K. Zhang, M. Shi, J. Xu, F. Liu, and K. Chen, “Force control for a rigid dual peg-in-hole assembly,” *Assem. Autom.*, 2017.
- [63] T. J. Debus, P. E. Dupont, and R. D. Howe, “Contact state estimation using multiple model estimation and hidden Markov models,” *Int. J. Rob. Res.*, vol. 23, no. 4–5, pp. 399–413, 2004.
- [64] Y. Wang *et al.*, “Contact Force/Torque Prediction and Analysis Model for Large Length-diameter Ratio Peg-in-hole Assembly,” in *2018 IEEE International Conference on Robotics and Biomimetics, ROBIO 2018*, 2019.
- [65] “Smooth-On, Dragon Skin™ A20.” [Online]. Available: <https://www.smooth->

on.com/products/dragon-skin-20/. [Accessed: 15-Nov-2019].

- [66] “Magfine, Φ 4mm x 2mm Neodymium Magnet Datasheet.” [Online]. Available: https://www.magfine.co.jp/products/detail.php?product_id=4368. [Accessed: 15-Nov-2019].
- [67] R. O. S. Wiki, “ROS (Robot Operating System) Documentation.” [Online]. Available: <http://wiki.ros.org>. [Accessed: 23-Nov-2019].
- [68] “Melexis, MLX90393 Triaxis.” [Online]. Available: <https://www.melexis.com/en/product/MLX90393/Triaxis-Micropower-Magnetometer>. [Accessed: 15-Nov-2019].
- [69] D. Guo, F. Sun, B. Fang, C. Yang, and N. Xi, “Robotic grasping using visual and tactile sensing,” *Inf. Sci. (Ny)*, vol. 417, pp. 274–286, 2017.